Stratified Flow Over Topography:
The Role of Small Scale Entrainment and Mixing in Flow Establishment

David Farmer[1] and Laurence Armi[2]

Submitted to Philosophical Transactions of the Royal Society: Physical Sciences and Engineering, December 31, 1997; in revised form, 22 July 1998.

[1]Institute of Ocean Sciences, Sidney, B.C., V8l4B2 Canada
[2]Scripps Institution of Oceanography, La Jolla, California, 92093-0230 USA

PAGE 35 + 36

IS

MISSING

IN

ORIGINAL

DOCUMENT

Table of Contents

Abstract:

Stratified flow over topography is examined in the context of its establishment from rest. A key element of numerical and steady state analytical solutions for large amplitude topographic flow is the splitting of streamlines which then enclose a trapped wedge of mixed fluid above the rapidly moving deeper layer. Measurements have been acquired which show that this wedge arises from small scale instabilities and mixing formed initially by the acceleration of subcritical stratified flow over the obstacle crest. The volume of trapped fluid progressively increases with time, permitting the primary flow to descend beneath it over the lee face of the obstacle. Throughout the evolution of this flow, small scale instability and consequent entrainment is the mechanism responsible for producing the weakly stratified wedge, thus allowing establishment of the downslope flow to take place. Velocity structure of instabilities within the entrainment zone is observed and the associated entrainment rate determined. The entrainment is sufficient to produce a slow downstream motion within the upper layer and a density step between the layers that decreases with downstream distance. The resulting internal hydraulic response is explained in terms of a theory which accommodates the spatially variable density difference across the sheared interface. The measurements described here were acquired in a coastal inlet subject to gradually changing tidal currents. It is proposed that the observed mechanism for flow establishment also has application to atmospheric flow over mountains.

1. Introduction

Stratified flow over topography has attracted attention for many reasons. These include forecasting severe downslope winds, clear air turbulence and the computation of form drag acting on the general circulation of the atmosphere for which topographic effects account for approximately 50% (Baines, 1995). It is also hypothesised to be a significant source of mixing in the ocean (Munk 1966, Armi 1978, Munk & Wunsch, 1998). A characteristic of many finite amplitude flows is the splitting of streamlines which then enclose a slowly moving or stagnant intermediate layer. This has been observed in atmospheric flows over mountains (Lilly 1978), in tidally forced oceanographic flows (Farmer & Smith, 1980) and has been reproduced in numerical models (Peltier and Clark, 1979).

Long's (1955) seminal laboratory and analytical studies of stratified flow over topography provide a natural starting point for this topic. Figure 1a illustrates a particular case in which the accelerated flow passing over the crest of an obstacle descends as a jet beneath a slow recirculation. A solution to Long's nonlinear theory corresponding to this case is shown beneath. Although closed streamlines violate the model assumptions, the solution is quite similar to the impulsively started laboratory result. Long's model has provided deep insight, but the solutions are nevertheless quite restricted in their application to geophysical flows because they are steady state and subject to specific upstream conditions.

Special solutions for steady state flow have been found which incorporate stagnant fluid. An idealised similarity solution for the case of stratified flow through a contraction (Figure 2) was first given by Wood (1968) and a special solution of Long's equation for flow over a ridge (Figure 3) is given by Smith (1985). The topic is also reviewed by Gill (1982), Wurtele, Sharman & Datta (1996), and Baines (1995). Streamline splitting is also apparent in the laboratory measurements of Long (1955), Baines (1977) and Armi & Williams (1993).

Figure 4(a-c) shows numerical solutions given by Peltier & Clark (1979) which address the establishment of this mixed region. These results were generally consistent with the observations of Lilly (1978). In this case, in which the isentropes are progressively distorted due to flow over a mountain, Peltier & Clark identify breaking of the large scale lee wave (Figure 4b) as the primary mechanism for mixing. The rapid drop in isentropes in the lee of the obstacle results in a high drag state. It has not been possible thus far to obtain geophysical measurements with the necessary time and space resolution to identify unambiguously the mechanisms leading to such flow structures. Aside from limitations in the spatial resolution of available atmospheric measurements, information is generally lacking with respect to their temporal evolution.

In the special case of a layered flow that is very slowly accelerated, diverging streamlines may adjust to equilibrium for given upstream conditions by flux within the dilating layer to produce this large volume of nearly stationary fluid, without any mixing taking place. This is an advective process which must be distinguished from the more general case of streamline splitting in a continuously stratified flow; the latter can take place only by back filling from the downstream reservoir or by mixing of the incoming flow. In the present study we show that small scale instability and entrainment plays a central role in the development and maintenance of the flow. As pointed out by Peltier & Clark (1979), the atmospheric observations lack the resolution necessary to determine the processes associated with the formation of this mixed region and there has been some controversy as to the nature of the relevant mechanisms (Lilly 1978, Lilly & Klemp 1980, Peltier & Clark 1980.). Lilly & Klemp (1980), for example, commented on the occurrence of wave induced shear instability, pointing out that the spatial scale of the turbulence differed substantially from that of the driving wave. Peltier & Clark (1980) emphasise the importance of breaking of the internal wave, while acknowledging that there are no observational data that can resolve this issue.

The present study discusses a well defined geophysical example of topographic flow allowing detailed examination of the processes responsible for generating the nearly stagnant weakly stratified layer. The measurements were acquired in an oceanographic context which is nevertheless dynamically similar to atmospheric flow over mountains. In the oceanographic context the fluid dynamical mechanisms discussed here are also of intrinsic interest, both as an energetic coastal process responsible for generation of non-linear internal waves and bores and as a possible source of mixing (Farmer & Freeland, 1983). The observations are intermediate in scale between laboratory ($Re \sim 10^4$ to 10^5) and atmospheric ($Re \sim 5x10^{10}$) flows, whereas numerical models are typically run with a numerical Reynolds number of 10^3. Although numerical models are essentially inviscid, they cannot resolve the small scale structure without resorting to special procedures such as nested grids (i.e. Scinocca & Peltier 1993). The present observations, which were acquired over a sill in an inlet with nearly exponential stratification, have a Reynolds number of 10^8. The ratio of the density gradient at depth to that aloft differs to some extent from the atmospheric case, but the general profile shape is similar and our observations allow detailed examination of the mechanisms leading to formation of these large weakly stratified regions. The Froude number of all these flows will also be seen to be comparable. We define Froude number in the usual layered hydraulic sense $F^2 = U^2 / g' h$, which in the uniformly stratified case is usually taken as $F=U/Nh$ where N is the buoyancy frequency, g' is the reduced gravitational acceleration and h is the fluid depth, whereas the inverse parameter Nh/U is often used in meteorology (and referred to as "Gnhu" by Baines, 1995).

The measurements were acquired in Knight Inlet, British Columbia (Figure 5), a fjord subject to strong barotropic flow due to a slowly varying tide. This inlet is approximately 120km long and is of relatively uniform width. A remnant moraine forms a sill within the straight reach of the inlet and it is the tidally forced flow, in particular the ebb tide when the current is towards the west, that is analysed here. The tide is predominantly semi-diurnal so that the half cycle corresponding to the ebb has a duration of approximately 6h. Just west of the sill the inlet widens significantly. In this respect the water motion takes on some of the characteristics of 'gap flows' characteristic of wind fields moving through mountain passes (Jackson & Steyn, 1994).

2. Observational Approach

The measurement approach is described in Figure 6. Observations were acquired from the Canadian Survey Ship VECTOR. In order to clarify the relative scales it should be pointed out that the aspect ratio of the background figure is 10:1. The vessel is drawn on a greatly enlarged scale at 1:1 aspect ratio, along with the distribution of sensors and acoustic beams; however the sensor distribution and acoustic beam orientation is preserved at the 10:1 aspect ratio in the lower portion of the figure so as to illustrate the quite fine spatial resolution of the measurements relative to the background flow. Ship position was continuously recorded using the Global Positioning System (GPS) with differential correction; all positions are referenced to the common ship track shown in Figure 5, with the origin at the sill crest and positive values downstream to the west. The example in Figure 6 is close to the strongest part of the ebb tide. A 120kHz echo sounder was used to acquire acoustical back scatter images, an example of which is shown as the background to Figure 6. Data from successive acoustic transmissions are acquired at uniform time intervals (0.5s) and are horizontally stretched or compressed in the figure so as to compensate for changing ship speed consistent with the horizontally uniform GPS referenced distance scale. This image is dominated by scatterers lying on a strongly stratified layer coincident with a shear zone separating nearly stationary fluid from the main flow. An array of up to 8 Inter Ocean S4 internally recording current meters and conductivity/temperature sensors were suspended from the vessel's bow. For many of the transects a conductivity-temperature-depth profiler (CTD) was continuously winched up and down from the stern while the ship was underway. Conductivity temperature and pressure measurements were used to derive the density field.

A 150kHz broad band Acoustic Doppler Current Profiler (ADCP) was used to acquire measurements of the current field. This instrument together with the echo-sounder transducer was mounted at a depth of 1m on a mast deployed over the side of the vessel on the starboard aft beam. The resulting distribution of velocity vectors and echo-sounder images shown in subsequent figures (i.e. Figure 7) is horizontally stretched or compressed in the same way by reference to the GPS determined positions for consistency with the linear distance scale. The inset in Figure 6 shows the instrument deployment configuration in plan view. The four ADCP beams point away from the ship's direction of travel. This arrangement minimises interaction between the ADCP acoustic beams and the towed instrumentation (S4 current meters and CTD profiler); occasionally contamination of the velocity signal can occur when there is a strong flow transverse to the direction of ship's travel and deeper instruments in the towed array drift sideways into one of the beams. These cases are readily identified and the corresponding velocity vectors have been deleted from the records (for example at 35m depth in Figure 7.1b). In contrast to the ADCP beams, the echo-sounder beam points straight down and quite frequently detects the deeper S4 current meters which are drawn aft during the more rapid traverses, appearing as nearly horizontal streaks in the images (i.e. at ~45m in Figure 6). A sidelobe reflection from the CTD may also be detected and helps to identify the instrument location relative to the echo-sounding image.

Three representative density profiles, expressed in the common oceanographic form[1] of σ_t and derived from continuous CTD profiles acquired as the ship traverses the sill, are shown in Figure 6. Density in these waters depends primarily on salinity, with temperature playing a secondary role. The paths followed by the CTD for each of the three density profiles in Figure 6 are shown as thick lines in Figure 7.4b. Density contours derived from the continuous CTD data are also shown in Figure 7.4b. The CTD profiles the water aft of the sonar mounted on the ship, introducing a small, depth dependent horizontal displacement relative to the sonar image. An offset of 10m, applicable to the upper 30m of the water column, has been made in the contour overlay. A similar effect is responsible for small discontinuities in the contours close to the surface (Figure 7b). Both the acoustical image and the other measurements are recorded as a time series along with GPS navigation data.

The scatter in the acoustical image in Figure 7 is due both to biota which tend to concentrate at density interfaces and also to sound speed gradients. The highly resolved images allow interpretation of distinctive signatures associated with distortion of the density field by the flow. The quantitative information to be derived from the images is positional change in the depth of isopycnals. In contrast to this quantitative result, the unknown combination of biological and physical factors contributing to acoustical cross-section make it difficult to derive quantitative estimates of processes directly related to the scattering mechanism, such as microstructure. Fish show up as discrete targets in several of the images.

---

[1] The density $\rho = 1000(1+\sigma_\tau)\mathrm{kg.m^{-3}}$.

An important simplification motivating the selection of this particular inlet is that during ebb tide, especially near the centre of the channel, the current from East to West results in a nearly 2-dimensional flow upstream and in the immediate vicinity of the sill. This 2-dimensional character breaks down near slack water and on the flood, accounting for our selection of ebb flows in the present discussion. Departures from a purely 2-dimensional flow are discussed in Sections 3 and 4.3, and illustrated in Figures 8 and 12c.

The Acoustic Doppler Current Profiler, manufactured by R.D.Instruments, uses the typical 4-beam Janus configuration. The forward and aft beams are oriented at 20deg to the vertical and are drawn beneath the enlarged sketch of the ship in the same aspect ratio as the image. Doppler velocity measurement of this kind is usually restricted to the horizontal components, but in the energetic environment with which we are concerned, vertical velocities may be substantial and have also been calculated. When the current field varies gradually in the horizontal relative to the separation of the beams, the calculated velocity vectors will be accurate. This assumption holds for most of our measurements; however, as discussed subsequently some care is required in analysing the derived velocity field of small scale structures on the interface. Due to sidelobe interference of the sloping beams, the ADCP does not provide useful profiles over the bottom 6% (i.e. $1-\text{Cos}20^{\text{o}}$) of the water column. This limit is identified on the accompanying figures by a light line above the sea floor.

The aspect ratio of Figure 6 and most subsequent figures is 10:1. The velocity field is shown in the form of 2-dimensional (i.e. vertical and downstream components) velocity vectors, coded with respect to magnitude and displayed with an orientation transformed to the same aspect ratio as the figures so as to illustrate the flow direction relative to that of the density contours and bottom slope. A consequence of this distortion is that the apparent angle of the strong downslope flow is exaggerated to match the scaling of the figure. Very weak flows near the surface may include small vertical components which similarly lead to steeply inclined vectors drawn in the 10:1 aspect ratio of this presentation, even though the true vertical velocities are typically much less than the horizontal components. The horizontal component of the vectors is resolved along the principal axis of the flow, which is closely aligned with the ship track shown in Figure 5. Only this component of the horizontal flow is shown in Figures 7.1b-7.6b; small cross stream components are illustrated and discussed subsequently.

3. Establishment and Evolution of the Flow

The acoustic imaging and velocity and density structure illustrated in Figure 6 serves as a framework for presentation of a sequence of traverses in Figures 7.1(a,b)-7.6(a,b) over the sill through the entire ebb tide so as to illustrate the gradual establishment and relaxation of the flow. For each traverse the acoustic image (a) is shown with the corresponding velocity vectors and density contours (b). The time span of the measurements is shown with reference to the tidal elevation in the inset to each figure.

The profiles in Figure 6 illustrate the strong surface stratification associated with fresh water run-off from the Klinaklini and Franklin rivers ~90km upstream at the head of the inlet. The Froude number calculated with respect to the thin surface layer is significantly less than unity, even in the rapidly moving flow over the sill crest. In this sense the near surface stratification also corresponds to the tropopause, as illustrated by the solutions of Peltier & Clark shown in Figure 4, although the relative stratification is stronger in the present case. The second profile in Figure 6 shows the presence of a relatively well mixed region from 5-15m over the sill crest. This corresponds to the mixed regions illustrated in Figures 3 and 4.

The ebb current is just beginning at the time corresponding to Figure 7.1, with most of the flow having a velocity less than 0.4ms^{-1}. Although no density profiles are available for this traverse, the near surface scattering layers are nearly horizontal showing only a weak response to flow over the sill.

In Figure 7.2 the density contours and scattering layers show a marked departure from the horizontal, both above and downstream of the crest. The velocity vectors and scattering layers further show that the flow follows the steep contour on the lee face of the sill, although separating at approximately 80m. Above the sill crest the acoustic image shows clear evidence of shear flow instabilities at 10-20m. At the downstream end of the unstable zone there is a discontinuity in scattering layer depth from 19m to 13m. In order to resolve the density field with greater horizontal resolution, the density contours in Figure 7.2b are derived from time series salinity-density measurements made with the towed sensors. The density contours slope gradually, but not abruptly upwards, in the vicinity of the depth discontinuity of the scattering layer mentioned above. It should be emphasised that the contour slopes in both Figures 7.2a and b are exaggerated due to the 10:1 aspect ratio of the presentation. We return to the detailed processes involved subsequently when we discuss Figure 10. Figure 7.2b also shows the beginnings of a weakly stratified layer at a depth of ~15m above the sill crest.

Four hours into the ebb flow (Figure 7.3) the weakly stratified layer has developed to nearly half the depth of the sill, with clear signs of shear flow instabilities reaching well upstream of the sill crest (-400m). This point also corresponds to the upstream limit of the isopycnal spreading shown in Figure 7.3b. The flow separates from the lee face of the sill at a depth of ~75m, after which it forms a coherently undulating jet between ~35m and ~70m. Above this jet the weakly stratified layer moves slowly downstream at 0.2-0.4ms^{-1}.

In Figure 7.4, approximately 5h into the ebb tide, the mixed region has deepened and a fully established downslope flow has formed in the lee. The flow does not separate in the immediate neighbourhood of the sill crest as seen previously. The isopycnals begin to spread still further upstream (-600m) and the deepening interface is again marked by shear flow instabilities. The slowly moving intermediate fluid exhibits weak stratification throughout and a pronounced oscillation occurs downstream of the crest. Again we see that there is a small net flow downstream within the partially mixed layer. Over the crest the interface lies at 30m and the jet achieves speeds of ~1ms^{-1}. Downstream of the crest the descending flow immediately above the sill reaches speeds of 1.2ms^{-1}.

Towards the end of the ebb tide (Figure 7.5), the current slackens and the thickness of the downslope flow decreases. However the interface continues to be contorted by instabilities. As discussed subsequently these instabilities result in entrainment. The effects of this continuing entrainment may also be seen and quantified through the progressive incorporation of acoustic scattering lines into the shear zone. For example, the 23σ_t isopycnal corresponds to a scattering layer appearing at 12m at the upstream edge of the image (-800m). Both the corresponding scattering layer and this isopycnal are incorporated into the shear zone just upstream (-100m) of the sill crest. Deeper isopycnals and scattering layers are entrained further downstream.

Figure 7.6 shows the relaxation of the ebb tide. The partially mixed layer has spread upstream in an exchange flow and only a weak descending current persists over the sill.

The horizontal and vertical components of all of the velocity vectors presented above have been resolved into the East-West component and the subsequent discussion takes the point of view that the flow is two-dimensional. The extent to which this simplification is justified is illustrated in Figure 8 where, in contrast to previous figures, we now show the horizontal orientation of the velocity vectors corresponding to Figure 7.3b. The flow upstream of the sill crest is very nearly due West. Over the sill the flow turns approximately 10^{o} to the North before returning to due West at position 500m. The small deviation over the sill crest is approximately in line with the orientation of the ship-track (Figure 5) and nearly orthogonal to the orientation of the sill crest. Our resolution of the current into the East-West component in Figures 7.1b-7.6b has the effect of understating the magnitude of the current by <2%. However we note that within the slowly moving and partially mixed flow at mid-depth above the sill crest, weak North-South flows occur. Some cross stream flow also occurs in the slowly moving water below the separation point in the lee of the sill. These exceptions are minor and in general the 2-dimensional representation appears to be well justified.

The observations in Figure 7 have been presented in some detail so as to provide the necessary background for the subsequent discussion. However, we emphasise that with respect to establishment of the flow, these results are by no means unique and indeed were observed to repeat with generally similar characteristics over other tidal cycles of comparable amplitude. It takes approximately 50 minutes to repeat each section so that some aspects of the transition are better illustrated from traverses acquired on other tides during the same cruise. For example, the time series for 26-27 August (Figure 10) discussed subsequently, is used to provided additional insight on instability and entrainment.

4. Interpretation

The essential characteristics of the observations presented above are identified in Figure 9. The initial response of the flow as it starts to move over the sill crest (Figure 9a) is a modest acceleration and an increase in shear near the surface together with a slight deepening of the near surface density contours. The subcritical response of a continuously stratified fluid is sheared (Pierrehumbert & Wyman, 1985). At some point internal waves develop in the neighbourhood of the crest. These waves grow and become unstable resulting in mixing (Figure 9b and Figure 7.2). Further entrainment allows the region of mixed fluid to thicken and extend downstream (Figure 9c and Figure 7.3). The thickening mixed layer eventually incorporates sufficient entrained fluid that a fully established hydraulically controlled flow develops (Figure 9d and Figure 7.4). Since this is a periodically forced flow we also observe its adjustment to decreased barotropic forcing through a deepening interface (Figure 7.5). Each of these aspects are discussed in detail below.

4.1 Initiation of Instability

The flow is accelerated as it moves up over the crest of the sill. This acceleration in a subcritical continuously stratified environment requires that the near surface stratification deepen and the velocity become sheared. The shear then leads to small scale instability. This aspect is best illustrated in Figure 10.1a,b where density, velocity and Richardson number profiles over the sill crest are shown for a traverse on 26 August, as the mixing begins. This development occurs at a tidal phase corresponding to a point intermediate between Figures 7.1 and 7.2. The Richardson number has been computed at the 2m vertical resolution of the velocity measurements and, as shown by the arrow, indicates marginal instability ($Ri \leq 0.25$) at the depth of the unstable flow. The shear resulting from subcritical response is distributed over >10m, so that the resolution of vertical current measurement is adequate for Richardson number calculations up to the point of instability. In the particular example illustrated here, we see no clear-cut evidence of overturning of the internal wave. Although there is evidence of small scale instability, the density profiles in particular do not show instability at the scale of the overall internal wave response.

4.2 Entrainment and Extension of Weakly Stratified Layer

In Figures 7.2-7.5 it is apparent that the progressively deepening interface is characterised by the presence of small scale shear instabilities. These occur above and upstream as well as downstream of the sill crest, typically having amplitudes of 1-5m, although reaching 10-15m downstream of the crest when the flow is fully established. They should be contrasted with the large amplitude (40-50m) undular jump ~200m downstream of the sill crest in Figures 7.3-7.5. These small scale instabilities occur simultaneously and within the overall development of the larger scale isopycnal distortion identified by Peltier and Clark (1979) as playing a dominant role in the *onset* of severe downslope wind formation. In the particular flow discussed here small scale instabilities are observed to occur at the onset of the response, as shown in Figure 10.1.

The small scale shear flow instabilities result in entrainment. The entrainment can be seen from the fine scale structure in the acoustic images. This is sketched in Figure 9b,c,d and is clearly visible in many of the images such as Figures 7.3-7.5. As a second example, which also illustrates the repetitive character of the response on each ebb tide, Figures 10.2 and 10.3 show the same behaviour following the initiation of instabilities illustrated in Figure 10.1 and discussed above. In both sets of examples the isopycnals (isentropes) are progressively incorporated into the entraining interface.

The entrainment is appropriately viewed in an isopycnal co-ordinate system. We define an entrainment ratio as $\varepsilon = \delta z/\delta s$, where δz is the vertical separation of two isopycnals upstream of the entrainment zone and δs is the distance along the entrainment zone separating the two locations at which these isopycnals are incorporated into the weakly stratified layer above the downslope flow. Values of the initial isopycnal depths and corresponding entrainment locations are shown for various examples in Figure 11. The slope of several points for each example then gives the entrainment ratio. For most of the entraining zone we find $\varepsilon \approx 0.02$, increasing in the steep portion downstream of the sill crest.

Our observations may be compared with laboratory measurements of entrainment into a gravity current reported by Ellison & Turner (1959) and discussed by Turner (1973). In contrast to these laboratory measurements in which the entrainment of fluid is downwards into the density current, our observations show an upwards entrainment from the downslope flow into the weakly stratified layer. This process has recently been observed in the laboratory for a spatially accelerated shear layer (Pawlak & Armi, 1999). As in the field measurements discussed above, the observed direction of entrainment was primarily upwards and is explained in terms of an appropriate stability analysis.

The weakly stratified layer continues to deepen (Figure 9c) and progressively increases in volume: the outflow from this layer moves slowly downstream above the entraining interface. Downstream of this entrainment zone (i.e. at 300m in Figure 7.3b and 7.4b), there is a net downstream flow within the partially mixed layer. Since the flow is essentially 2-dimensional, the only source of this outflow is the entrainment. Therefor the increasing volume of mixed fluid does not arise through back filling; on the contrary, some of the entrained fluid leaves the mixed region in the downstream direction.

We can check the continuity of the entrainment assumption from a simple integration over the progressively increasing area of the weakly stratified layer. From Figures 7.2, 7.3 and 7.4, we find that within the bounds of our measurement region, which terminates downstream at position 550m, the area of the weakly stratified layer increases at a rate of $\sim 4 m^2 s^{-1}$. The entrained flow rate per unit width is given by $\varepsilon \cdot \Delta u \cdot \Delta s$, where $\Delta u \approx 0.8 ms^{-1}$ is the velocity difference across the shear layer and $\Delta s \approx 600m$ is the length of the entraining zone. The resulting value is $\sim 10 m^2 s^{-1}$ between Figures 7.2 and 7.4, which is approximately twice the required filling rate. The excess must move downstream and it is clear, for example in Figure 7.3, that this is indeed occurring. The outflow speed in this case is $\sim 0.2 ms^{-1}$ acting over a depth of ~20m, which just balances the excess of the entrained flow over the increasing volume of the weakly stratified layer. It is certain that near the sides of the channel and further downstream 3-dimensional effects become important, but within the area of measurement the primary features satisfy continuity calculated within a 2-dimensional representation.

4.3 Structure of Entraining Eddies

The instabilities grow as they move along the sheared interface. The smaller scale structures appearing in Figures 7.4-7.5 cannot be well resolved in the images because of the large aspect ratio of the display required to encompass all of the key components of the response. In order to illustrate the detailed structure, a 1:1 aspect ratio expansion of a short section of unstable interface over the sloping lee face of the sill is shown in Figure 12a. This example is from 30 August and was selected because of the clarity of the expanded acoustic image and the increased size of the instabilities. Corresponding velocity vectors, derived from the vertical and downstream components are shown in Figure 12b, and from the two horizontal components in Figure 12c, analogous to Figure 8.

The entraining interface in this example is inclined at ~45degrees. Caution is required in the interpretation of the velocity measurements because the Doppler profiler configuration requires that the velocity components be derived from beams that are spatially separated.

The subtended angle of each beam is 20 degrees corresponding to a separation of 20m at a depth of 30m. Although the resolved velocity component along each sloping beam can be accurately determined, it is not possible to derive unambiguous estimates of the velocity at a resolution less that the separation scale. This only becomes an issue when we choose to display the observations from a highly variable field with greatly expanded resolution. It should be noted that velocity samples are calculated by the Doppler profiler at a significantly higher rate than the time it takes to traverse the measured field lying within the diverging beams, and in this figure we have displayed the resulting vectors at 5m horizontal spacing, so that the result is similar to the use of a horizontal running average, the scale of which increases with depth. Despite the ambiguities of the measurement at this high resolution, the velocity vectors are consistent with the coherent structures in the acoustic image.

A further subtlety in the interpretation of Figure 12 results from the fact that the measurements are acquired from a vessel travelling downstream at a speed of 0.6ms^{-1}, whereas the rapidly moving lower layer has a speed of 1.2ms^{-1}. Within the shear zone the velocity difference is of order 0.6ms^{-1} so that we expect the unstable structures to be moving downstream at approximately half this speed, say ~0.3ms^{-1}. Since this is one half of the ship's speed we expect Doppler stretching by a factor of two. However the Doppler stretching occurs primarily within the deeper (i.e. higher speed) portion of the shear zone and the crests of the instabilities lying within the weakly sheared flow remain relatively motionless. They have a wavelength of ~40m. The existence and theoretical basis of instabilities on a steeply inclined interface has recently been discussed by Pawlak and Armi (1998).

Wisps of acoustical back scatter of length ~10-20m can be observed leaving the crests of the instabilities. These wisps, presumably corresponding to entrainment, can be identified as vortical structures in the velocity vector field. Much smaller scale (~3-5m) variability can be observed on the primary scattering layer. We identify these as evidence of secondary instabilities which grow to form the next larger scale structure further downstream. These instabilities grow through vorticity generated by the baroclinic component of the shear. Figure 12c shows the corresponding cross-stream component of flow and it is evident that within the weakly stratified layer the large scale vortices become 3-dimensional. The flow in the deeper layer is towards the west. The only 3-dimensional structures appear in the wisps, at ~10m above the interface.

4.4 The Fully Established Stratified Flow and Relaxation

Figure 7.4b shows the fully established flow which is hydraulically controlled at the sill crest. It has taken 4 hours to entrain sufficient fluid into the weakly stratified layer to allow the fully established flow to occur. The primary current continues accelerating down the lee face of the sill for 200m downstream of the crest, after which it rebounds to form an undular internal hydraulic jump. The separation of the boundary layer from the lee face of the sill is now suppressed until the descent of the downslope flow is reversed by buoyancy forces due to the downstream conditions. This downslope flow and separation is very similar to the severe downslope winds modelled by Peltier & Clark (1979) reproduced in Figure 4c, and to the atmospheric observations of Lilly (1978).

Finally, over four hours after our first traverse, the barotropic forcing by the tide has slackened and the flow begins to relax. At this stage the flow does not simply follow in reverse the sequence occurring in the early stages of the forcing when it was of comparable magnitude, since the weakly stratified layer now exists. The decrease in barotropically forced flux results in a deepening of the interface at the crest consistent with maintenance of critical conditions. Eventually the forcing decreases to the point where the weakly stratified fluid above the interface starts to move in the opposite direction, forming an exchange flow (Figure 7.6). This mechanism has been discussed previously for the two-layer case by Farmer & Armi (1986).

4.5 The Weakly Stratified Layer

Returning now to the weakly stratified layer lying above the entraining interface, we note that the flow speeds are low and the entrained fluid moves downstream away from the entrainment zone. Except near the largest instabilities there is little sign of mixing within the weakly stratified layer. A consistent characteristic of the isopycnals within this layer is that they slope up towards the surface and gradually converge downstream. Although the resulting flow is continuously stratified, some insight may be derived by examining its behaviour in terms of a layered structure, in which each layer is bounded by isopycnals such as those shown in Figures 7.3b-7.7b. We consider the hydraulic state of one of these layers and focus on that portion lying above or upstream of the sill crest (for example in Figure 7.4). Taking the layers bounded by 0.5 sigma-t isopycnals, we find vertical separations of 3m to 10m and layer speeds of order 0.2-0.4ms^{-1}. This implies layer densimetric Froude numbers ($F_i^2 = U_i^2 / g'h_i$ where U is the layer speed, h the thickness and g' the reduced gravity) between 1 and 10, consistent with the observed supercritical response of acceleration and thinning as the isopycnals rise towards the surface and converge.

Eventually the accelerating near surface stratified flow must be matched to the downstream conditions. In general we did not observe the details of this matching, but in Figures 7.5a and 7.5b it is apparent that the near surface layer, bounded by isopycnals 20 and 22 σ_t, rapidly thickens, beginning at a location ~175m downstream of the sill crest. This behaviour is characteristic of an internal hydraulic jump that matches the thin supercritical flow near the surface to the thicker subcritical layer downstream. An important consequence of the horizontal stratification in this slowly moving layer is that the deeper flow is subject to an interfacial density step that progressively decreases with distance downstream. As discussed subsequently, this changing density step modifies the behaviour of the deeper layer.

4.6 The Downslope Flow

Thus far the hydrostatic assumption has been implicit in our discussion. However, downstream of the control, vertical acceleration is non-negligible and becomes apparent in the undular character of the flow. This property is related to an important problem in atmosphere dynamics: the penetration of the downslope flow into the pool of fluid beneath, which may be denser (Lee et al, 1989). In the atmosphere its importance relates to the depth to which severe downslope winds extend.

Beyond the penetration, the interface between the partially mixed layer and the downslope flow (Figure 7.4) rises rapidly in an internal undular hydraulic jump. Although not described as such, a similar structure appears to be present in the data of Lilly (1978) downstream of Boulder where significant turbulence was also noted. As an atmospheric comparison it is interesting to note that the kinetic energy of the downslope flow per unit volume (ρu^2) during severe downslope winds observed in Boulder (Lilly, 1978) is approximately the same as the present observations.

The essential characteristics of the flow may be summarised as follows. Stratified water accelerates as it moves up over the sill, with the greatest shear occurring nearer the surface. This shear enhancement is consistent with layered hydraulic models (see Baines, 1995, Fig. 5.41a). The sheared flow results in instability and entrainment which produces a weakly stratified layer overlying the primary flow. Initially this flow separates from the crest of the obstacle, but as the weakly stratified layer fills in through entrainment, the separation is suppressed and the rapidly moving flow plunges down the lee face of the obstacle in qualitative consistency with predictions of Peltier & Clark (1979), Smith

(1985) and Baines (1995). The continuous model of Smith (1985) and the layered model of Baines (1995) would need some modification to account for the continuously varying entrainment across the interface and resultant variations of the weakly stratified layer. Although slowly moving, the weakly stratified flow is initially supercritical, thus accounting for the progressive rise and convergence of adjacent isopycnals. Thus the flow consists of two regions of continuously stratified hydraulic response separated by an entrainment zone. The entraining process is associated with relatively small scale overturning eddies that produce only local mixing.

5 Hydraulic Analysis

Our observations provide a basis for comparison with previous model analyses of topographic flows. An appropriate approach to this is through the framework of internal hydraulics. In Section 5.1 we discuss the relationship between Long's model, Smith's solution and reduced gravity hydraulic flows. We derive the theory for a homogenous layer descending beneath a passive layer in which the density varies with position, and compare the results with our observations. In section 5.2 we summarise the components of a gradually varying model that leads to fully established flow. Although the different parts of this model are identified, it is apparent that they are all coupled, so that an analytical description is intractable. However, identification of the essential components and their inter-relationship serves as a prescription for further numerical studies.

5.1 Steady State Analyses

Long's model, which gives exact steady solutions for larger values of Nh/U, where $N = \left(-\frac{g}{\rho}\frac{d\rho}{dz} \right)^{1/2}$ is the buoyancy frequency with g the gravitational acceleration and ρ the density, h is the obstacle height and U the upstream velocity, has been very widely used in the study of finite amplitude stratified flow over topography. This model is closely related to the hydraulic interpretation which underlies the present discussion. Since Long's model does not allow streamline separation, the solutions can only approximate observations where recirculating flow actually occurs. The nonlinear equation describing the flow can be transformed into the Helmholtz equation for the special case $dq/dz = 0$ where

$q = \rho_0(z_0)U(z_0)^2/2$ and $\rho_0(z_0)$ and $U(z_0)$ are the upstream density and velocity profiles respectively. Under these conditions,

$$\nabla^2\delta + \kappa^2\delta = 0 \qquad (1)$$

where

$$\kappa^2 = N(z_0)^2 / U(z_0)^2 = -g\frac{d\rho_0}{dz}/2q, \qquad (2)$$

κ is constant for constant $d\rho_0 / dz$ and δ is the vertical displacement of the streamlines. If ρ is approximately constant so that the Boussinesq approximation is applicable, *N(z)* and *U(z)* are effectively constant. Long's implicit approach to solutions has been greatly extended to include a variety of obstacle shapes (c.f. Huppert & Miles, 1969, Lilly & Klemp, 1979). A relevant example (Figure 1) adapted from Long's (1955) original paper shows the flow accelerating over the crest to form a jet running down the lee face of the obstacle. This jet is overlain here by a recirculating flow approximated by the closed streamline. Even though closed streamline flow violates the model assumptions, the solution is qualitatively consistent with laboratory flows near the sill crest.

An important modification was applied to Long's model by Smith (1985). For the hydrostatic case (1) simplifies to

$$\frac{\partial^2\delta}{\partial z^2} + \kappa^2\delta = 0. \qquad (3)$$

Smith (1985) found a hydrostatic solution for the special case of a pliant upper boundary condition expressed as

$$u = U, \quad \frac{\partial \delta}{\delta z} = 0, \text{ at } z = D + \delta_T . \qquad (4)$$

In (4), D is the upstream elevation of the separation streamline and δ_T its vertical displacement after separation. If the solution is expressed in terms of a Froude number $F^2 = \pi\ U / 2ND$, it is apparent that for the given upstream conditions, the only solutions that are controlled (i.e. $F^2 = 1$) at the obstacle crest are those which result in an asymmetrical response. The first mode solution, applicable in the present case, is shown in Figure 3. As discussed by Baines (1995), this asymmetry in the flow is hydraulic in character.

Although Smith's solution provides a qualitative understanding of the downslope wind problem, it still contains an arbitrary selection of upstream conditions which mean that it cannot be applied to real flows without some *a priori* assumptions. This was recognised by Smith who described his result as primarily a consistency analysis. Specifically, in order to solve Long's equations, the point at which the calculation of $y(x)$ or $\delta_T(x)$ begins is by necessity chosen at the beginning of the obstacle. For a single layer hydraulic analysis Farmer & Armi (1986) showed that the location of the tip of the wedge depends upon the barotropic forcing. Smith's solution also assumes that the density step is negligible, but as shown in the observations above and further discussed below, the spatial variability of the density step is not known *a priori* and may be significant.

An internal hydraulic analysis in its usual form is not appropriate for the flows discussed here, since the background stratification has a significant influence on the response. The flow may be divided into a deeper accelerating layer of nearly uniform density, and a weakly stratified upper layer. The streamline split occurs within the strongly stratified portion of the upstream density profile. In consequence the accelerating layer carries with it a thin stratified cap which is eroded by entrainment. This stratified cap is only a few metres thick (~7% of the upstream thickness of the lower layer) and therefor has negligible direct effect on the overall energetics of the lower layer. However, the entrainment over time of this stratified cap into the upper layer provides a changing density step between the two layers which must be accounted for in the internal hydraulic analysis. Although not completely stagnant, the upper layer moves slowly. For example, a Froude number calculation at the control point above the sill crest based on the depth averaged velocity and density of the lower layer and the measured interfacial density step, together with the upper layer velocity, shows that $F_1^2 < 0.1$. We are therefor justified in approximating the upper layer as being passive. This simplification results in a single layer hydraulic flow subject to a horizontally varying density step.

A modified Bernoulli equation for a single layer of thickness y moving over an obstacle of height h, subject to a varying reduced gravitational acceleration $g' = g'(x) = g\frac{\Delta\rho(x)}{\rho}$, can be expressed as

$$\frac{u^2}{2g'y_c} + \hat{y} + \hat{h} = \hat{H}, \tag{5}$$

where we have normalised all elevations y, h, H, by the thickness y_c of the moving layer at the crest. The dimensional continuity equation $q = u \cdot y$ could be readily adapted to include the small loss of fluid through entrainment to the upper layer, but this is negligible and will not be carried through in what follows. Incorporating the continuity equation in the critical condition at the sill crest, leads to

$$F_c^2 = \frac{q^2}{g'_c \cdot y_c^3} = 1, \tag{6}$$

where the subscript c denotes the crest location. From (5) and (6) we derive the non-dimensional equation for single layer flow beneath a wedge of horizontally varying density:

$$\frac{1}{2\hat{g} \cdot \hat{y}^2} + \hat{y} + \hat{h} = \hat{H}. \tag{7}$$

In (7) we normalise the reduced gravity by its value over the crest: $\hat{g}(x) = g'(x) / g'_c$. Referencing all values to the critical point at the crest leads to $\hat{y} = 1$, $\hat{g} = 1$ and $\hat{h} = 0$, so that $\hat{H} = \frac{3}{2}$.

For the special case of classical single layer hydraulics, $\hat{g} = 1$ everywhere and (7) predicts the additional points shown in Figure 3. The equivalent hydraulic result almost coincides with Smith's solution, as expected on the basis of Durran & Klemp's (1987) analytic comparison. Deviation at the upstream end can be accounted for by the fact that Smith's solution assumes a uniform upstream velocity field, which then yields a sheared flow downstream of the streamline bifurcation. The result is therefor not self-similar as required for a hydraulic solution and a calculation proceeding upstream from the crest leads to the observed deviation. However, the agreement is close over much of the solution range. Due to its self-similar structure, Wood's (1968) solution for flow through a contraction has behaviour identical to that of a single layer passing through a contraction.

The solution for variable background density is now applied to our observations of the established flow. Equation (7) is evaluated for the measured topography (*h*), depth averaged flow speed (*u*) and density, together with the density step ($\Delta\sigma_t$), for several positions (*x*) in Figure 7.4. The result (y_{calc}), given in Table I and plotted in Figure 13, is consistent with the observed interfacial displacement (*y*), within the limits of our ability to measure the relevant variables. (The measurements are insufficiently accurate for carried out with a multiple layered hydraulic model approximating the upstream conditions (see, for example, Baines, 1995, section 5.9).

The resulting instabilities lead to mixing and the mixed fluid is trapped above the sill. Before this mixing takes place, the exchange of potential for kinetic energy required for the flow to accelerate over the sill comes from a small dilation of the brackish surface layer which remains subcritical at all times, as prescribed by the equations of internal hydraulics. Once entrainment has begun, the mixed region rapidly increases in size and, except for the processes of entrainment, decouples the moving layer beneath from the fluid lying above. At this point the deeper layer remains subcritical and the depth of the unstable interface is determined by the downstream conditions. Flow separation occurs, as observed in Figures 7.3, 10.2, 10.3 and sketched in Figure 9b,c. With increasing time the weakly stratified layer fills in, the lower layer accelerates, an asymmetric interface shape forms and control is established near the sill crest. The flow continues to separate from the crest until the weakly stratified layer deepens sufficiently to establish an asymmetrical structure resulting in a favourable pressure gradient.

A crucial aspect of the time dependent response is the rate at which the weakly stratified layer fills in. This is determined by the difference between the rate at which the layer is formed through entrainment and the rate at which it leaves downstream. The rate and manner of this downstream movement of the weakly stratified layer will be determined in part by the time dependent downstream conditions.

Figure 14, which is adapted from Figure 7.4b, identifies the essential components that must be included in a comprehensive model after entrainment begins and the weakly stratified layer is formed. Upstream of the wedge of weakly stratified fluid, the flow will follow that expected for a subcritical stratified response. The fact that it is subcritical means that its behaviour depends upon the downstream state which includes, for example, the shape and position of the wedge of weakly stratified fluid described by Figure 9. It is characteristic of this problem that each component of the model representation illustrated in Figure 14 is coupled and the entire problem must be calculated simultaneously. An unstable entraining interface couples the accelerating deeper flow above the crest to the weakly stratified layer above. Since fluid is entrained by small scale instabilities across this interface, it must intersect isopycnals and does so at an angle determined by the entrainment ratio. The deeper water accelerates and moves down the lee face of the sill, making a smooth transition from subcritical to supercritical flow at the control above the sill crest. Except in the vicinity of the entraining interface, this flow could also be adequately described by a multi-layered hydraulic model. However, as discussed above, the density of the fluid above the entraining interface changes with position, and this continuous stratification modifies the density step between the deeper and upper layers, thus influencing the hydraulic response. At some point well downstream of the crest the lower layer rebounds in an internal hydraulic jump to match the downstream conditions.

An important characteristic of the entraining interface is that in general the instabilities are relatively small. Consequently the entraining interface does not mix the entire layer behind it. There are no obvious signs of large scale overturning within this weakly stratified layer.

An internal hydraulic jump matches the supercritical downslope flow to the depth of the interface bounding the weakly stratified layer. This jump is a dominant feature in Figures 7.4 and 7.5 where it assumes an undular form. The flow in the weakly stratified layer above must also match the downstream conditions as may be seen, for example, in Figure 7.5.

6 Concluding Remarks

The observations and analysis presented above show the mechanisms that lead to establishment of stratified flow over topography (Figure 9). Small scale shear instabilities appear to be responsible for the initial phase of mixing above the obstacle crest. This mixing leads to a slowly moving, weakly stratified layer that progressively increases in volume with time and is bounded beneath by a density step. This step is a necessary consequence of entrainment. Initially the deeper layer separates from the sill crest. Formation of the weakly stratified layer is necessary for deepening and acceleration of the lower layer. This acceleration in turn produces a favourable pressure gradient at the crest, suppressing separation and leading to fully established downslope flow.

The stability of stratified flow over mountains has also been studied in great detail with numerical (Peltier & Clark, 1979) and analytical (Laprise & Peltier, 1989) models. As pointed out by Scinocca & Peltier (1989), Peltier & Scinocca (1990) and Peltier (1993) Kelvin-Helmholtz instabilities may be generated along the downslope interface (see also Smith, 1991, Fiedler, 1992, Smith 1992). Scinocca and Peltier (1993) in particular have carried out a very high resolution calculation with a triple nested grid that provides a useful comparison and contrast with our observations. The model takes Long's solution as an initial condition which is then forced at uniform speed and shows Kelvin-Helmholtz instabilities beneath the weakly stratified layer at a later time in the fully developed windstorm. The instabilities are clearly entraining fluid into the mixing region not unlike those shown in Figure 12.

Smith's (1985) special solution of Long's equations shown in Figure 3 illustrates the accelerating flow but differs in an important way from the case discussed here and indeed from any case in which the overlying layer is formed by mixing of the incoming fluid, since entrainment across the bounding interface forms a density step, apparent in our observations. The density step changes with position depending upon the upstream stratification, the entrainment rate and the dynamics of the weakly stratified layer. Progressive decrease in the magnitude of the step results in a thicker and more slowly moving downslope flow than would otherwise be the case. This solution is limited to constant $N(z)$ and $\rho U^2(z)$ which restricts its applicability to real flows in contrast to the self-similar streamline splitting solutions for contractions discussed by Wood (1968) and Armi & Williams (1993).

A distinguishing feature of many previous studies of finite amplitude stratified flow over topography has been the application of Long's model, either as an initial condition for numerical computations or for the derivation of analytical solutions (i.e. Smith 1985). However Pierrehumbert & Wyman (1985) and Garner (1995) carried out detailed numerical calculations and showed that upstream influence was a significant factor at lower Froude numbers. The flows studied here start from rest, i.e. *low* Froude numbers using the hydraulic definition, and are gradually accelerated. The time scale for the response to change in forcing therefor becomes a relevant variable. In the analysis of any real flow it is necessary to consider the relative time scales for set up of the flow and for the escape of upstream disturbances. In our case the wave propagation speed is ~1m/s and the obstacle length scale is ~1km giving an escape time for the upstream influence of order 1000s. Since this is short compared to the relevant time scale of tidal effects (~10,000s), upstream influence cannot be ignored. As a representative atmospheric example, we note that a length scale of 300km and wave speed of 30m/s give an escape time of 10^4s or ~3h. Only for extremely rapid passage of a front is the set-up time scale shorter than 3h. Thus we may also expect upstream influence to be relevant to atmospheric flow over mountains.

Our observations and analysis have focused on the examination of the gradual evolution of these flows and show unambiguously that it is small scale instability above and in the neighbourhood of the obstacle crest that is initially responsible for the mixing. This instability arises from shear due to upstream influence of subcritical flow over the obstacle. This is distinct from the instability found in Long's solution and is instead a subcritical hydraulic response, which serves to emphasise that the upstream conditions cannot be prescribed without taking the time evolution of the flow into account. In the natural atmospheric or oceanographic environment, impulsive flow must be relatively rare, so that the gradually increasing flow speed and associated evolution discussed above provides a more representative picture.

Acknowledgements

We thank the officers and crew of the CSS VECTOR for their assistance in the field program. We acknowledge helpful comments provided by Dick Peltier, John Scinocca and Peter Baines. We are also indebted to those who helped with different aspects of the field program and data analysis, especially Matt Grinder, Nancy Hurlbirt, Grace Kamitakahara-King, Geno Pawlak, Rich Pawlowicz, Dan O'Brien and Les Spearing. The Acoustic Doppler Profiler was provided by Eric D'Asaro. We are grateful to the U.S. Office of Naval Research for financial support.

References

Armi, L. 1978 Some evidence for boundary mixing in the deep ocean *J. Geophys. Res.* **83** 1971-1979.

Armi, L & Williams, R. 1993 The hydraulics of a stratified fluid flowing through a contraction *J. Fluid Mech.* **251** 355-375.

Baines, P. G. 1995 *Topographic effects in stratified flows*, 482pp., Cambridge University Press.

Baines, P.G. 1977 Upstream influence and Long's model in stratified flows *J. Fluid Mech.* **82** 147-159.

Durran, D.R. and Klemp, J.B., 1987 Another look at Downslope Winds. Part II: Nonlinear Amplification beneath Wave-Overturning Layers *J. Atmos. Sci.* **44** 3402-3412.

Ellison, T.H. & Turner, J.S. 1959 Turbulent entrainment in stratified flows *J. Fluid Mech.* **6** 423-448.

Farmer, D.M. & Armi, L. 1986 Maximal two-layer exchange over a sill and through the combination of a sill and contraction with barotropic flow *J. Fluid Mech.* **164** 53-76.

Farmer, D.M. & J. Dungan Smith 1980 Tidal interaction of stratified flow with a sill in Knight Inlet *Deep Sea Res.* **27A** 239-254.

Farmer, D.M. & Freeland, H.J. 1983 The physical oceanography of fjiords *Progress in Oceanography* **12** 147-219.

Fiedler, B.H. 1992 Comments on "Kelvin-Helmholtz instability in severe downslope wind flow *J. Atmos. Sci.* **49** 2343-2344.

Garner, S.T., 1995 Permanent and Transient Upstream Effects in Nonlinear Stratified Flow over a Ridge *J. Atmos. Sci.* **52** 227-246.

Gill, A. E. 1982 *Atmosphere-Ocean Dynamics*, 662pp., Academic Press.

Huppert, H.E., and Miles, J.W. 1969 Lee waves in a stratified flow. Part 3. Semi-elliptical obstacle. *J.Fluid Mech.* **35** 481-496.

Jackson. P.L. & Steyn, D.G. 1994 Gap winds in a fjord, Part I: Observations and numerical simulation *Mon. Wea. Rev.* **122** 2645-2665.

Laprise, R. & Peltier, W.R. 1989 The linear stability of nonlinear mountain waves: implications for the understanding of severe downslope windstorms *J. Atmos. Sci.* **46** 545-564.

Lee, T.J. Pielke, R.A., Kessler, R.C. & J Weaver 1989 Influence of cold pools downstream of mountain barriers on downslope winds and flushing *J. Atmos. Sci.* **117** 2041-2058.

Lilly, D.K. 1978 A severe downslope windstorm and aircraft turbulence event induced by a mountain wave *J. Atmos. Sci.* **35** 59-77.

Lilly, D.K. & Klemp, J.B. 1979 The effects of terrain shape on mountain waves *J. Fluid Mech.* **95** 241-262.

Lilly, D.K. & Klemp, J.B. 1980 Comments on "The evolution and stability of finite-amplitude mountain waves. Part II: Surface wave drag and severe downslope windstorms *J. Atmos. Sci.* **37** 2119-2125.

Long, R.R. 1955 Some aspects of the flow of stratified fluids. Part III: Continuous density gradient *Tellus* 7 341-357.

Munk, W. 1966 Abyssal recipes *Deep Sea Res.* **13** 707-730.

Munk, W. & Wunsch, C. 1998 The moon and mixing: abyssal recipes II. To appear: *Deep Sea Research.*

Pawlak, G. & L. Armi 1999 Vortex dynamics in a spatially accelerating shear layer. In press: *J. Fluid Mech.*

Peltier, W.R. (1993) Reply, *J. Atmos. Sci.* **50** 3034-3040.

Peltier, W.R., & Clark, T. L. 1979 The evolution and stability of finite-amplitude mountain waves. Part II. Surface wave drag and severe downslope windstorms *J. Atmos. Sci.* **36** 1498-1529.

Peltier, W.R., & Scinocca, J.F. 1990 The origin of severe downslope windsorm pulsations *J. Atmos. Sci.* **47** 2853-2870.

Pierrehumbert, R.T. & Wyman, B. 1985 Upstream effects of mesoscale mountains, *J. Atmos. Sci.* **42** 977-1003.

Scinocca, J.F. & Peltier, W.R. 1989 Pulsating downslope windstorms, *J. Atmos. Sci.* **46** 2885-2914.

Scinocca, J.F. & Peltier, W.R. 1993 The instability of Long's stationary solution and the evolution toward severe downslope windstorm flow. Part I: Nested Grid Numerical solutions *J. Atmos. Sci.* **50** 2245-2263.

Smith, R.B. 1985 On severe downslope winds. *J. Atmos. Sci.* **42** 2597-2603.

Smith, R.B. 1991 Kelvin-Helmholtz instability in severe downslope wind flow *J. Atmos. Sci.* **48** 1319-1324.

Smith, R.B. 1992 Reply *J. Atmos. Sci.* **49** 2345-2346.

Turner, J.S. 1973 Buoyancy effects in fluids. Cambridge University Press, 367 pp.

Wood, I. R. 1968 Selective withdrawal from a stably stratified fluid *J. Fluid Mech.* **32** 209-223.

Wurtele, M.G., Sharman, R.D. & Datta, A. 1996 Atmospheric Lee Waves *Annual Rev. Fluid Mech.* **28** 429-476.

Table I

$x(m)$	$h(m)$	$\Delta\sigma_t$	$u(ms^{-1})$	F^2	$y(m)$	$y_{calc}(m)$	$y_{\Delta fixed}(m)$
-600	8	7.0	0.55	0.07	63	65	57
-500	-6	6.0	0.60	0.10	61	62	55
-400	-4	5.0	0.62	0.13	58	60	52
-300	-3	4.5	0.65	0.17	56	58	50
-200	-1	3.0	0.70	0.33	50	53	44
-100	*	2.0	0.80	0.74	43	*	*
-65	0	1.7	0.83	1.16	39	*Critical*	*Position*
0	-2	1.5	0.95	1.7	35	38	33
50	-9	1.2	1.04	2.6	35	37	27
100	-26	0.8	1.0	3.7	34	36	22

Table I. Observed interface depth *(h)*, density step $(\Delta\sigma_t)$, flow speed *(u)*, Froude number (F^2), lower layer thickness: observed *y(m)*, derived from equation (7) and y_{calc}, derived from (7) for constant $\Delta\sigma_t$, $y_{\Delta fixed}$. All values expressed as a function of position *x*.

Figure captions

1. Long's (1955) laboratory visualisation and calculation of flow over an obstacle.

2. Wood's (1968) self-similar solution for steady stratified flow with an arbitrary density profile moving from an infinite reservoir through a horizontal contraction. *Above:* Elevation view showing the initial density profile in the reservoir to the left, the vertical displacement of the streamlines, and the stagnant fluid above and beneath the moving fluid. *Below:* Plan view showing reservoir and withdrawal area downstream of the narrowest section.

3. Smith's (1985) solution for steady, continuously stratified flow over a mountain with uniform flow upstream. The solution includes stagnant fluid in a wedge above the descending flow. Points have been added to indicate a single layer hydraulic solution with no stratification in the moving layer.

4. Numerical solutions of Peltier & Clark (1979) showing isentrope fields for a wind storm simulation at (a) 4160s, (b) 5120s and (c) 8000s after initial conditions.

5. Chart of Knight Inlet, British Columbia. Large Inset: Bathymetry in neighbourhood of the sill with depths are given in metres. The straight line shown across the sill corresponds to the ship track followed in observations described subsequently. Small Inset:

Representative acoustic image from a ship traverse. Note that this and all subsequent images are shown as though viewed in elevation from the North such that the ebb tidal current flows from left to right.

6. Sketch showing measurement approach. The vessel (37m length shown here greatly enlarged) supports an acoustic Doppler profiler, echo-sounder, towed S4 current meter/CTD array and towed profiling CTD. The sketch is superimposed on an acoustic image made by the echo-sounder. A portion of the echo-sounding image, showing as horizontal lines at 45m, is contaminated by sidelobe reflections from the towed S4 array. The echo-sounding image is reproduced in colour in Figure 7.4a. *Inset:* Plan view of vessel showing acoustic Doppler beams and towed instrumentation.

7.1a-7.6a Acoustic images through an ebb tide sequence. *Inset:* Shows the time of the measrement relative to tidal phase.

7.1b-7.6b For each corresponding image in Figure 7a and using the same aspect ratio, Doppler velocity vectors, coded as to magnitude, are shown for the vertical and downstream components. Contours of constant density are shown where available.

8. Horizontal acoustic Doppler vectors corresponding to Figure 7.3, derived from the *cross-track* and *downstream* velocity components so as to show the hrrizontal direction of the flow. The orientation of the horizontal component of the current is illustrated for each vector as though it were shown in plan view from above, as illustrated in the inset. The

nearly horizontal orientation of the vectors shows that the dominant flow direction is to the West.

9a-e. Schematic diagram summarising the time dependent response for stratified flow over topography discussed in the text.

10.1a Acoustic image of flow over the sill crest in the early stages of the ebb current, illustrating initial development of shear flow instabilities. Density and velocity profiles are shown for the upstream *(left)* and sill crest *(right)* locations. Richardson numbers are calculated from the velocity and density profiles acquired immediately above the sill crest. The horizontal arrow identifies location of the Richardson number profile.

10.1b Density contours and velocity vectors corresponding to Figure 10.1a.

10.2a, 10.3a Acoustic images of the developing weakly stratified layer continuing through the ebb tide sequence that begins in Figure 10.1a.

10.2b, 103b Density contours and velocity vectors corresponding to Figure 10.2a, 10.3a.

11. Calculation of entrainment ratio as defined in the text. Each point represents a particular isopycnal from the corresponding density contours for stated times. The ordinate gives the upstream depth of the isopycnal while the abscissa identifies the

horizontal location at which the isopycnal is incorporated in the entraining flow. The entrainment ratio is defined as the slope of a set of such points.

12a Acoustic image of instabilities in the entrainment zone shown at 1:1 aspect ratio.

12b Velocity field corresponding to Figure 12a.

12c Horizontal velocity components only, corresponding to Figure 12a, shown using same convention as for Figure 8. Vectors pointing to the right indicate a current *downstream*, while vertical vectors indicate *cross-track* flow.

13. Hydraulic analysis of the flow shown in Figure 7.4. The dots show the theoretically predicted interface locations for the measured density differences shown. The dashed curve shows the prediction for a fixed density step corresponding to that measured at the sill crest. The solid curve shows the observed interface location. The size of the observed density step at different locations is expressed in $\Delta\sigma_t$ (see text). Froude numbers from the measured data for the accelerated layer are plotted below.

14. Essential components of a comprehensive model for continuously stratified flow over topography (adapted from 7.4b).

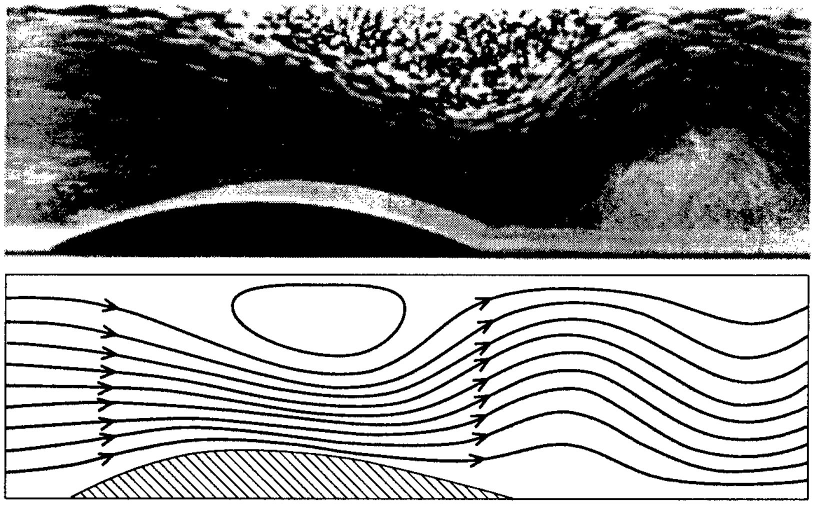

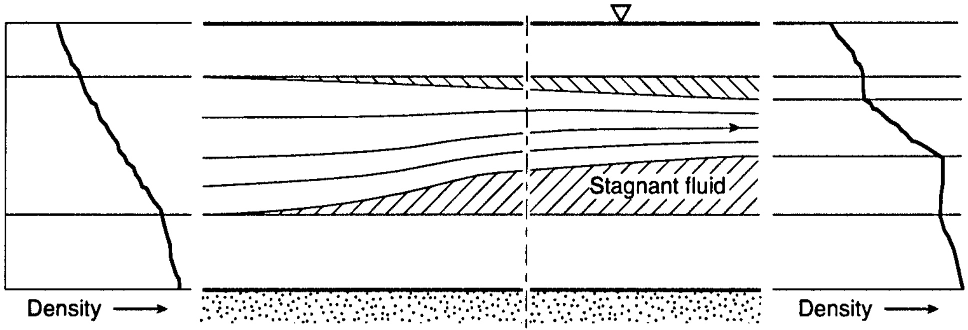

Elevation

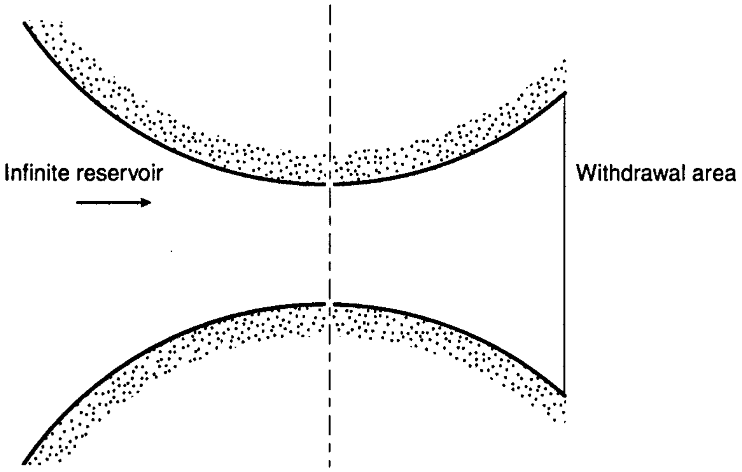

Plan

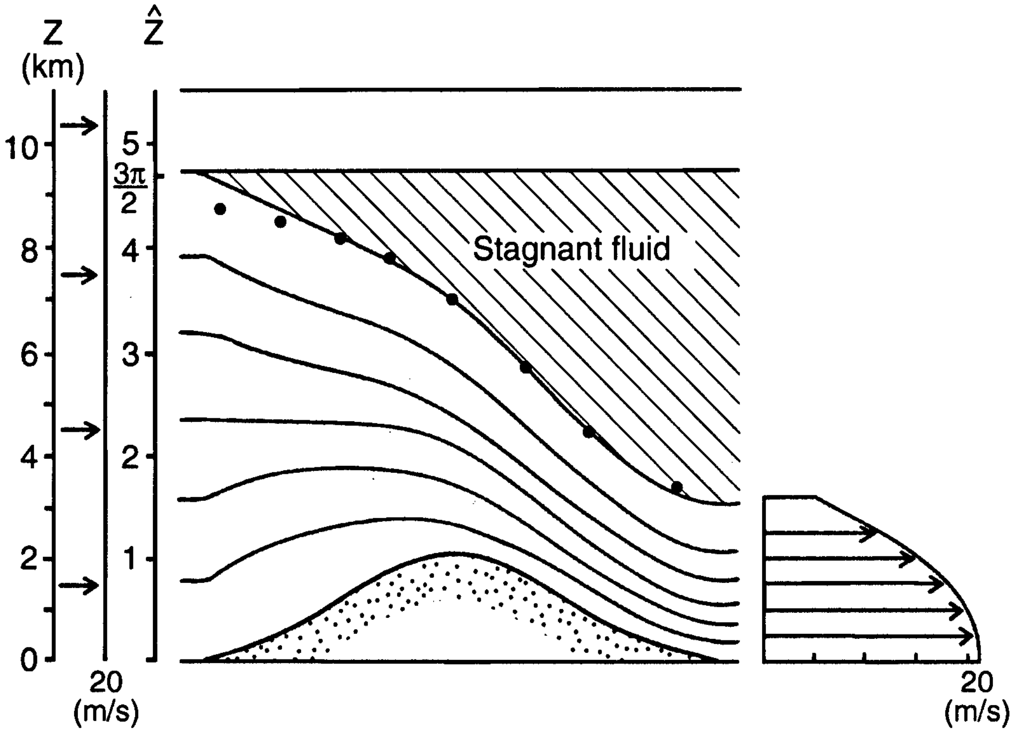

Z
(km)
Ẑ
10
8
6
4
2
0
5
$\frac{3\pi}{2}$
4
3
2
1
20
(m/s)
Stagnant fluid
20
(m/s)

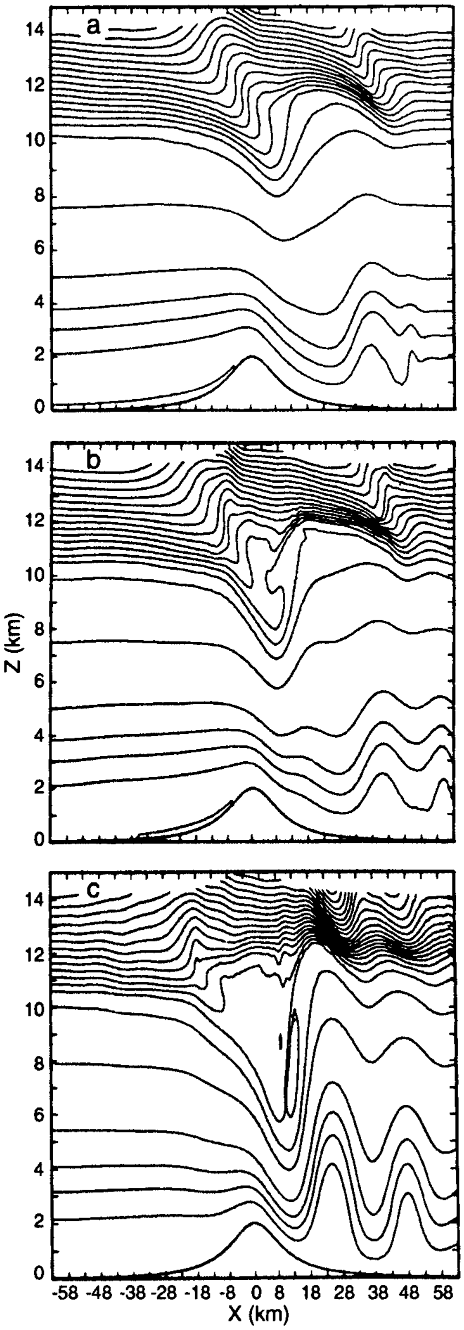
a
b
c
14
12
10
8
6
4
2
0
Z (km)
-58 -48 -38 -28 -18 -8 0 8 18 28 38 48 58
X (km)
1

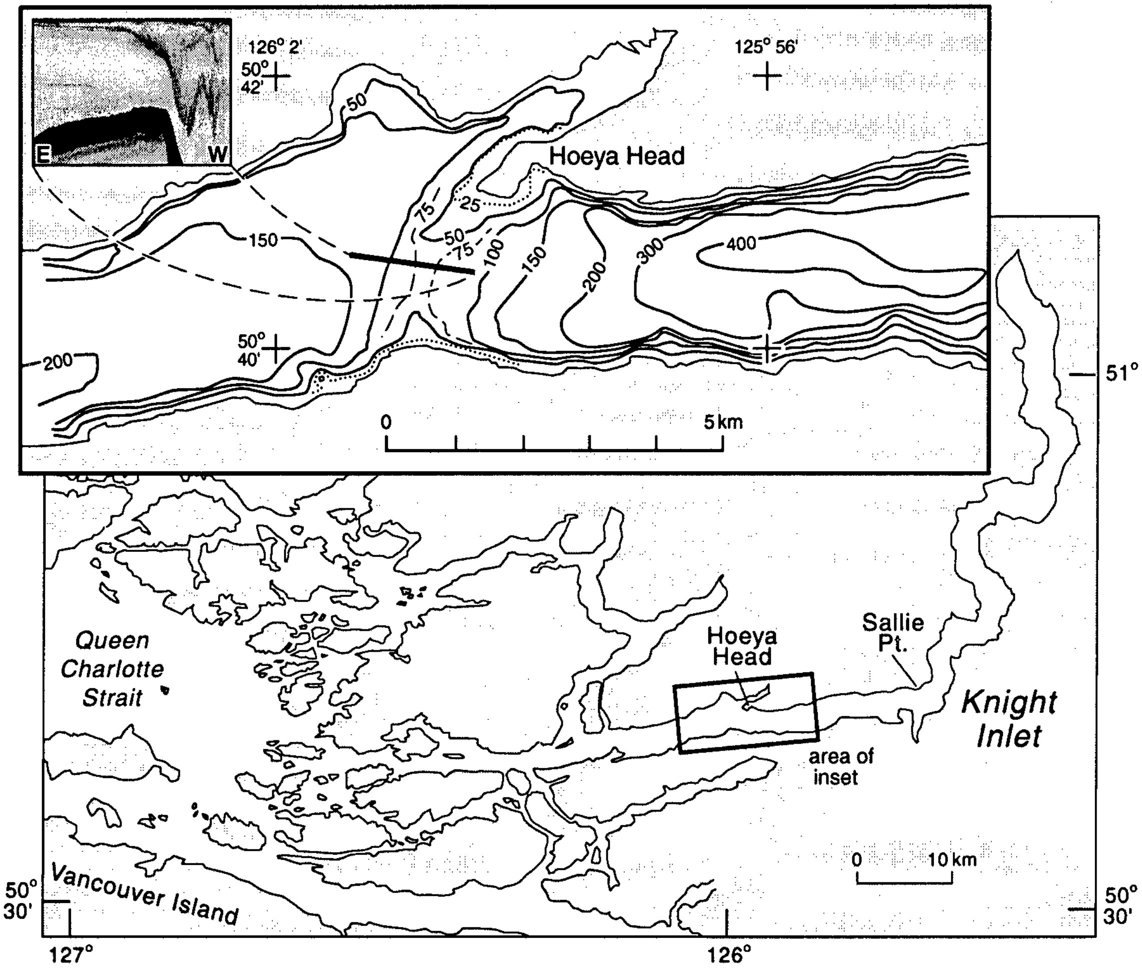
E
W
126° 2'
50°
42'
125° 56'
50
Hoeya Head
25
75
50
75
100
150
200
300
400
150
50°
40'
200
0
5 km
Queen
Charlotte
Strait
Hoeya
Head
Sallie
Pt.
Knight
Inlet
area of
inset
0
10 km
51°
50°
30'
50°
30'
Vancouver Island
127°
126°

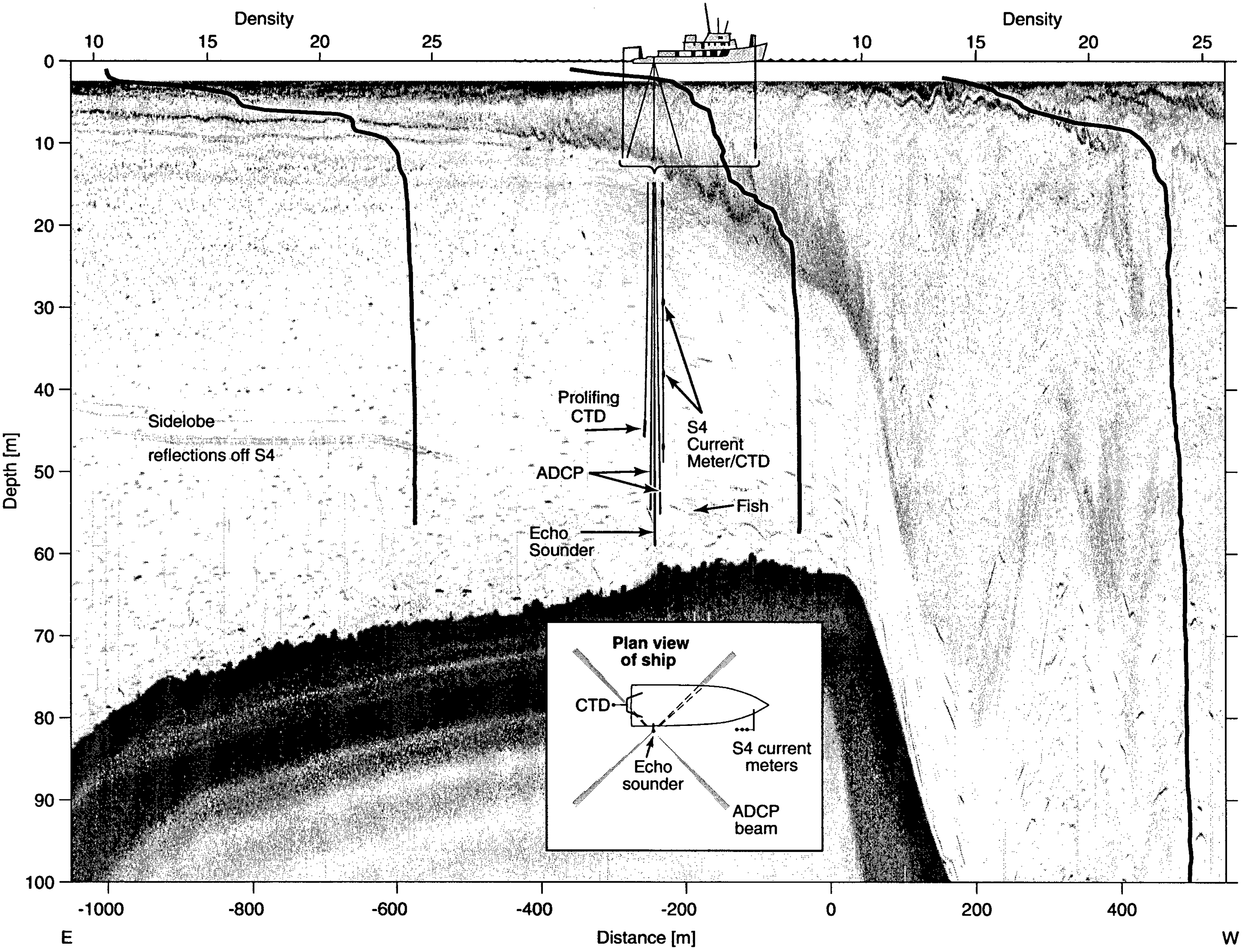
Density
10
15
20
25
Density
10
15
20
25
Density
15
20
25
Depth [m]
0
10
20
30
40
50
60
70
80
90
100
Sidelobe
reflections off S4
Prolifing
CTD
ADCP
Echo
Sounder
S4
Current
Meter/CTD
Fish
Plan view
of ship
CTD
Echo
sounder
S4 current
meters
ADCP
beam
-1000
-800
-600
-400
-200
0
200
400
E
Distance [m]
W

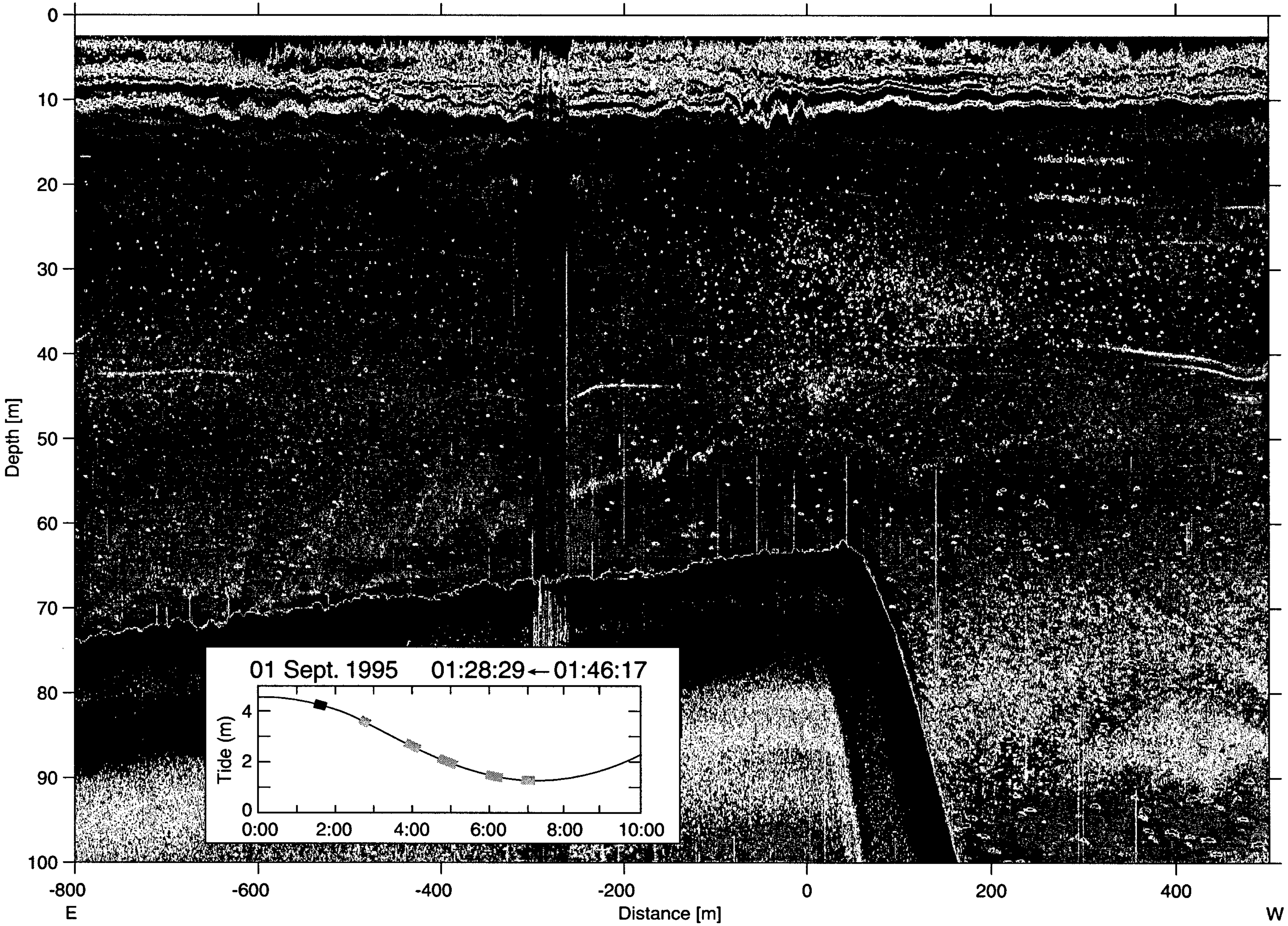
0
10
20
30
40
50
60
70
80
90
100
Depth [m]
-800
-600
-400
-200
0
200
400
E
Distance [m]
W
01 Sept. 1995 01:28:29←01:46:17
Tide (m)
0
2
4
0:00
2:00
4:00
6:00
8:00
10:00

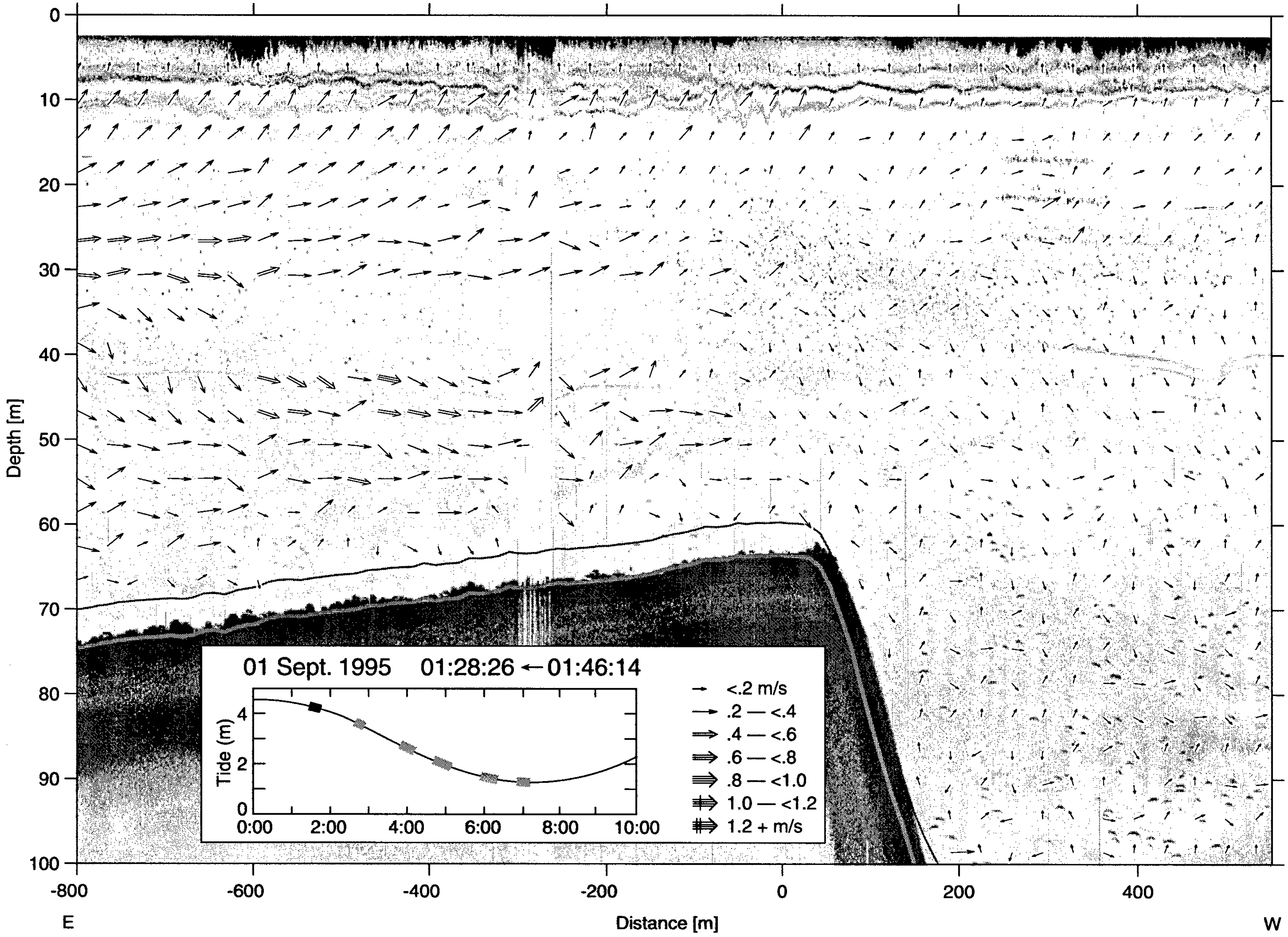
0
10
20
30
40
50
60
70
80
90
100
Depth [m]
-800
-600
-400
-200
0
200
400
E
Distance [m]
W
01 Sept. 1995 01:28:26 ← 01:46:14
Tide (m)
4
2
0
0:00
2:00
4:00
6:00
8:00
10:00
<.2 m/s
.2 — <.4
.4 — <.6
.6 — <.8
.8 — <1.0
1.0 — <1.2
1.2 + m/s


Depth [m]
0
10
20
30
40
50
60
70
80
90
100
Distance [m]
-800
-600
-400
-200
0
200
400
E
W
01 Sept. 1995 02:39:10→02:53:30
Tide (m)
0
2
4
0:00
2:00
4:00
6:00
8:00
10:00

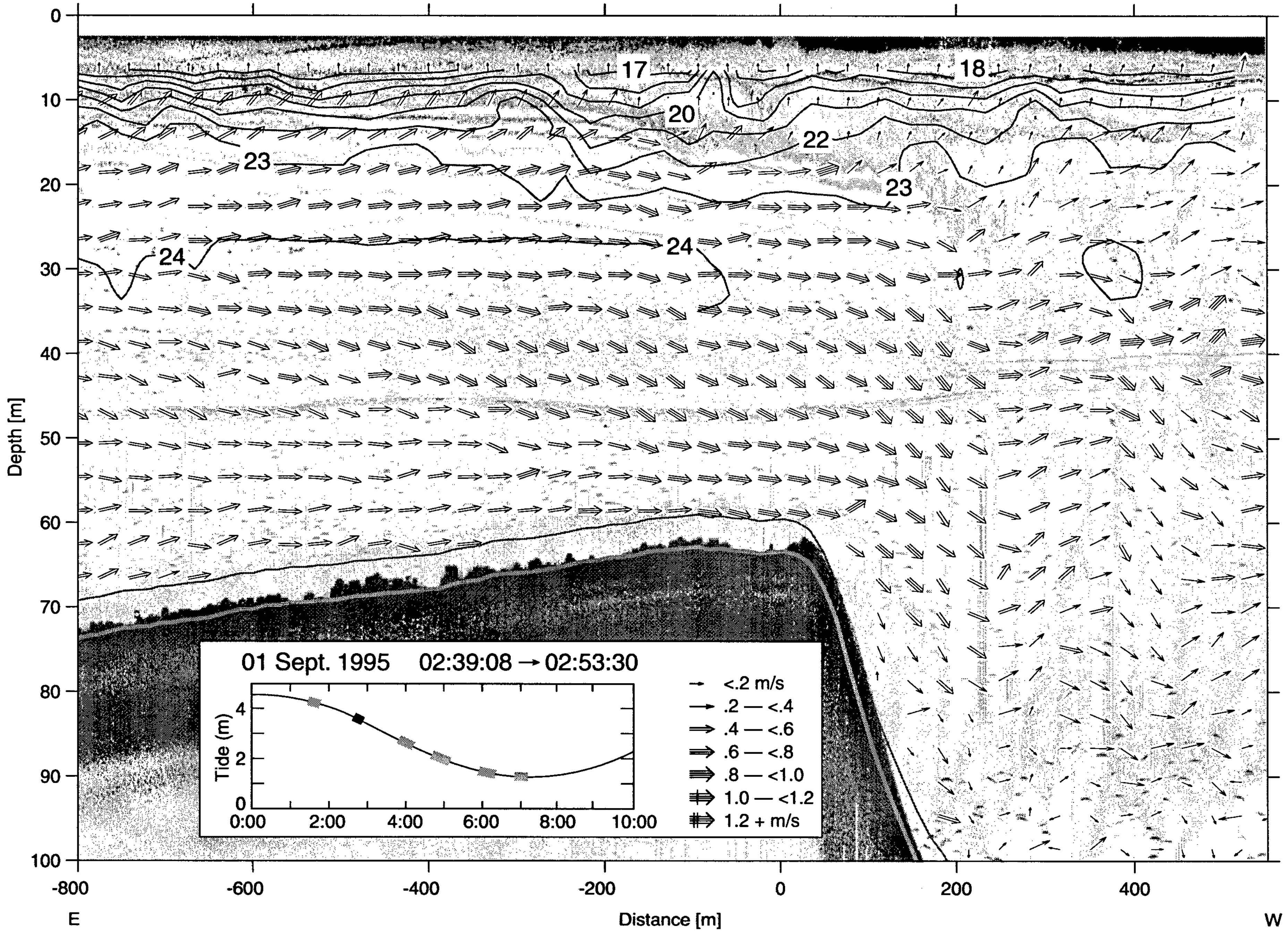

01 Sept. 1995 02:39:08 → 02:53:30
Tide (m)
0
2
4
0:00
2:00
4:00
6:00
8:00
10:00
<.2 m/s
.2 — <.4
.4 — <.6
.6 — <.8
.8 — <1.0
1.0 — <1.2
1.2 + m/s
17
18
20
22
23
23
24
24
Depth [m]
0
10
20
30
40
50
60
70
80
90
100
-800
-600
-400
-200
0
200
400
Distance [m]
E
W

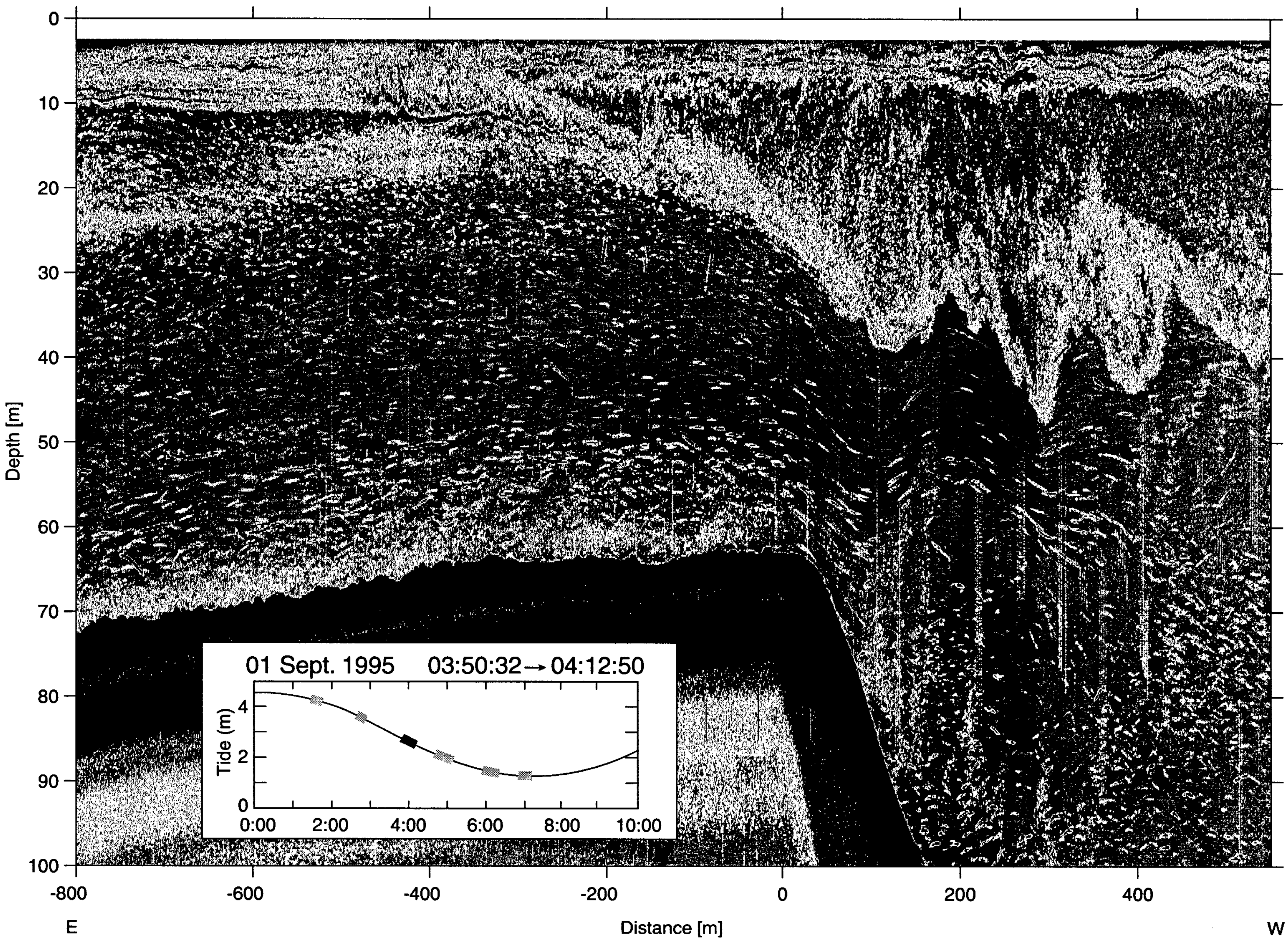
01 Sept. 1995 03:50:32→04:12:50
Tide (m)
0
2
4
0:00
2:00
4:00
6:00
8:00
10:00
Depth [m]
0
10
20
30
40
50
60
70
80
90
100
-800
-600
-400
-200
0
200
400
E
Distance [m]
W

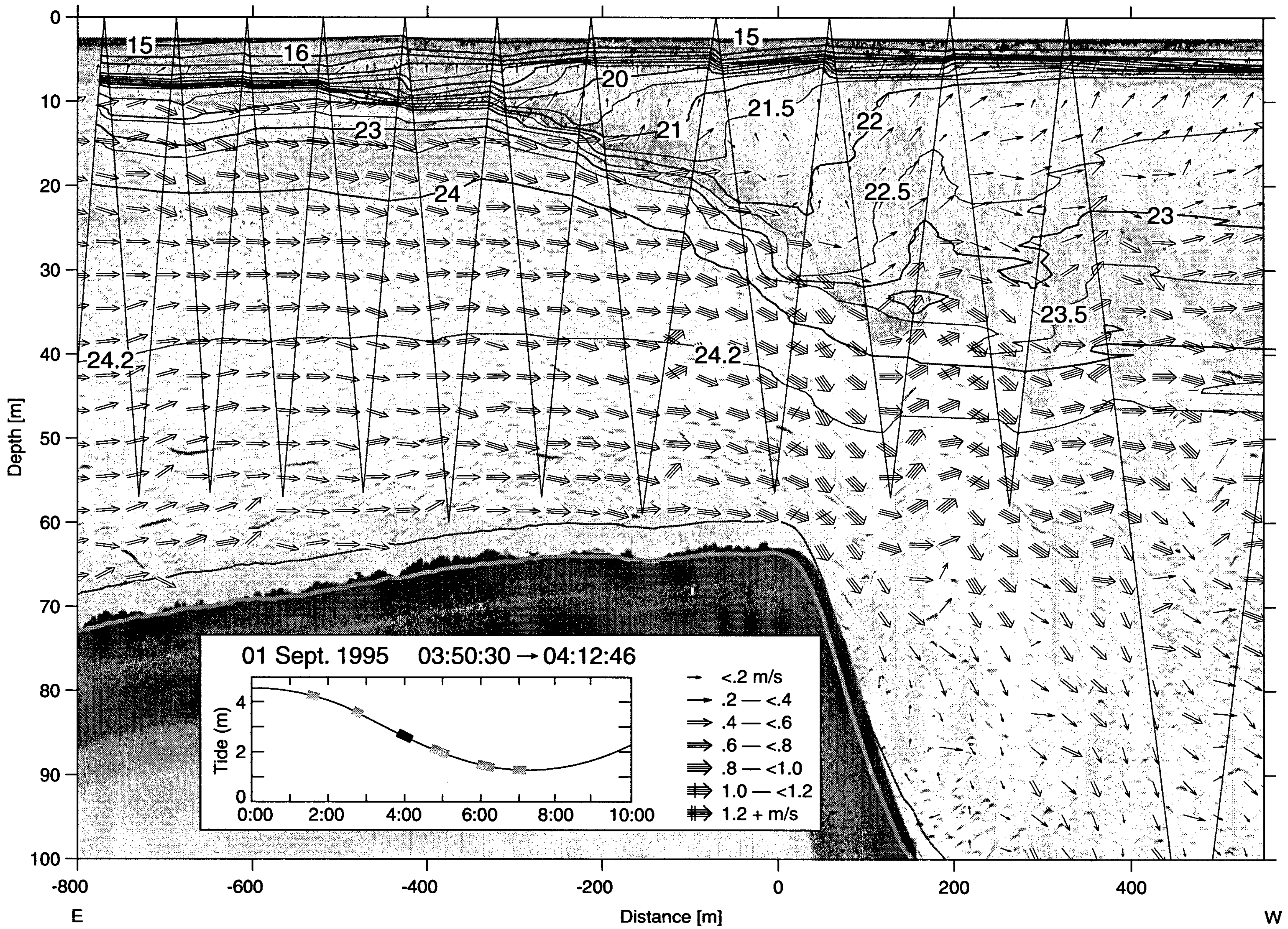
01 Sept. 1995 03:50:30 → 04:12:46
Tide (m)
0:00
2:00
4:00
6:00
8:00
10:00
<.2 m/s
.2 — <.4
.4 — <.6
.6 — <.8
.8 — <1.0
1.0 — <1.2
1.2 + m/s
15
16
20
21
21.5
22
22.5
23
23.5
24
24.2
Depth [m]
Distance [m]
E
W
-800
-600
-400
-200
0
200
400
0
10
20
30
40
50
60
70
80
90
100

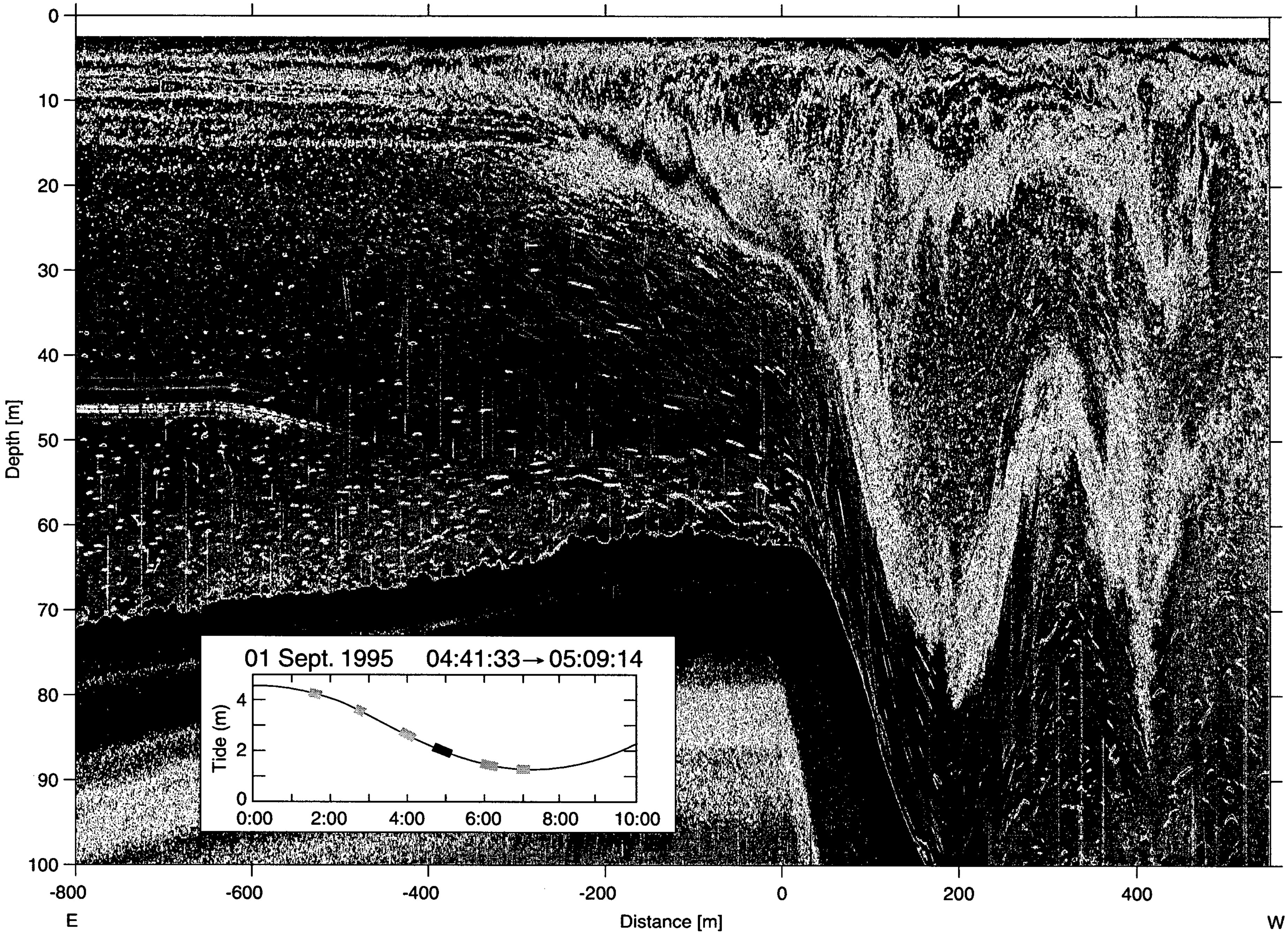

0
10
20
30
40
50
60
70
80
90
100
Depth [m]
-800
-600
-400
-200
0
200
400
E
W
Distance [m]
01 Sept. 1995 04:41:33→05:09:14
Tide (m)
0
2
4
0:00
2:00
4:00
6:00
8:00
10:00

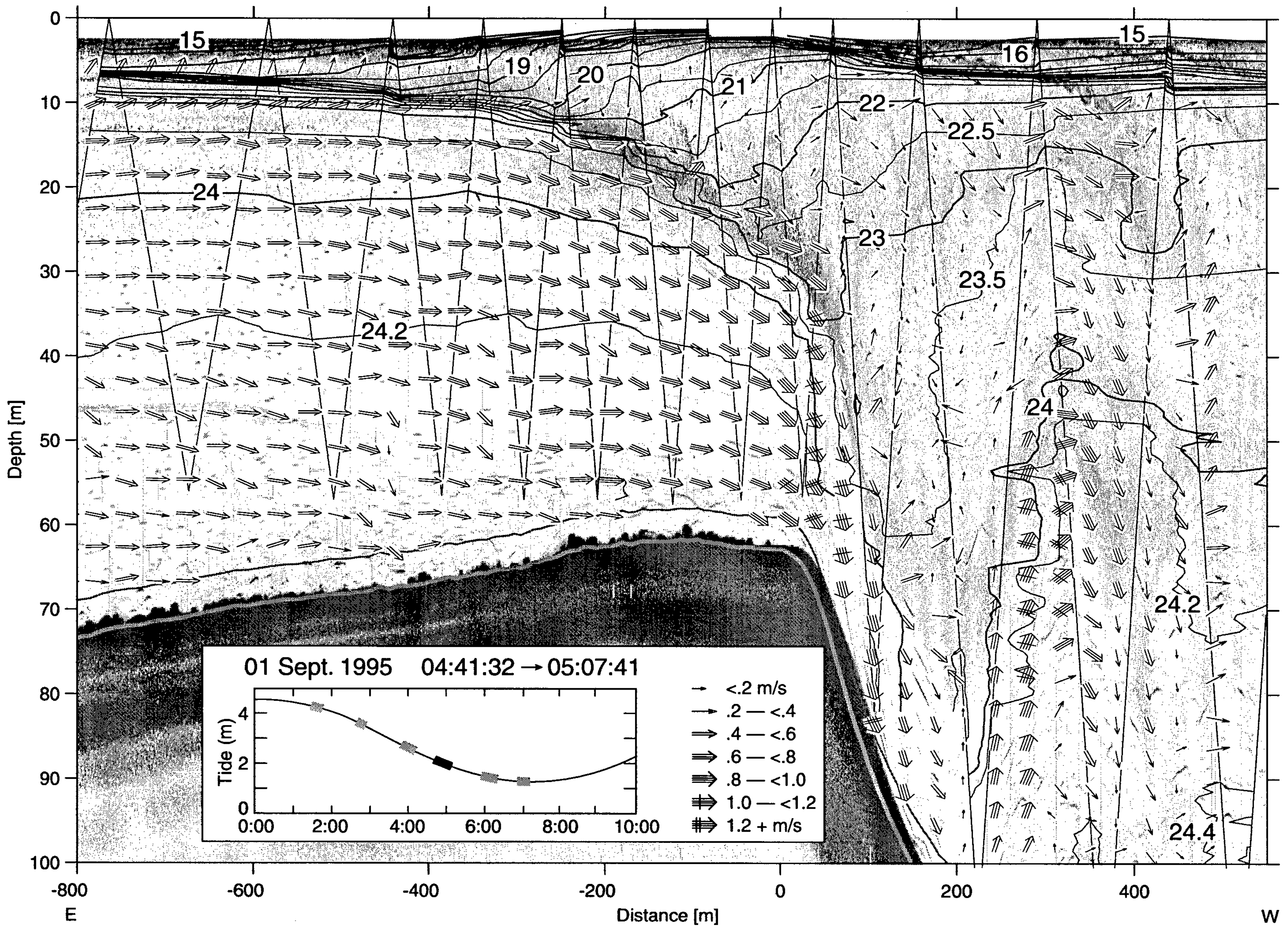
0
10
20
30
40
50
60
70
80
90
100
Depth [m]
-800
-600
-400
-200
0
200
400
E
W
Distance [m]
15
19
20
21
22
22.5
23
23.5
24
24.2
16
15
24
24.2
24.4
01 Sept. 1995 04:41:32 → 05:07:41
Tide (m)
0
2
4
0:00
2:00
4:00
6:00
8:00
10:00
<.2 m/s
.2 — <.4
.4 — <.6
.6 — <.8
.8 — <1.0
1.0 — <1.2
1.2 + m/s

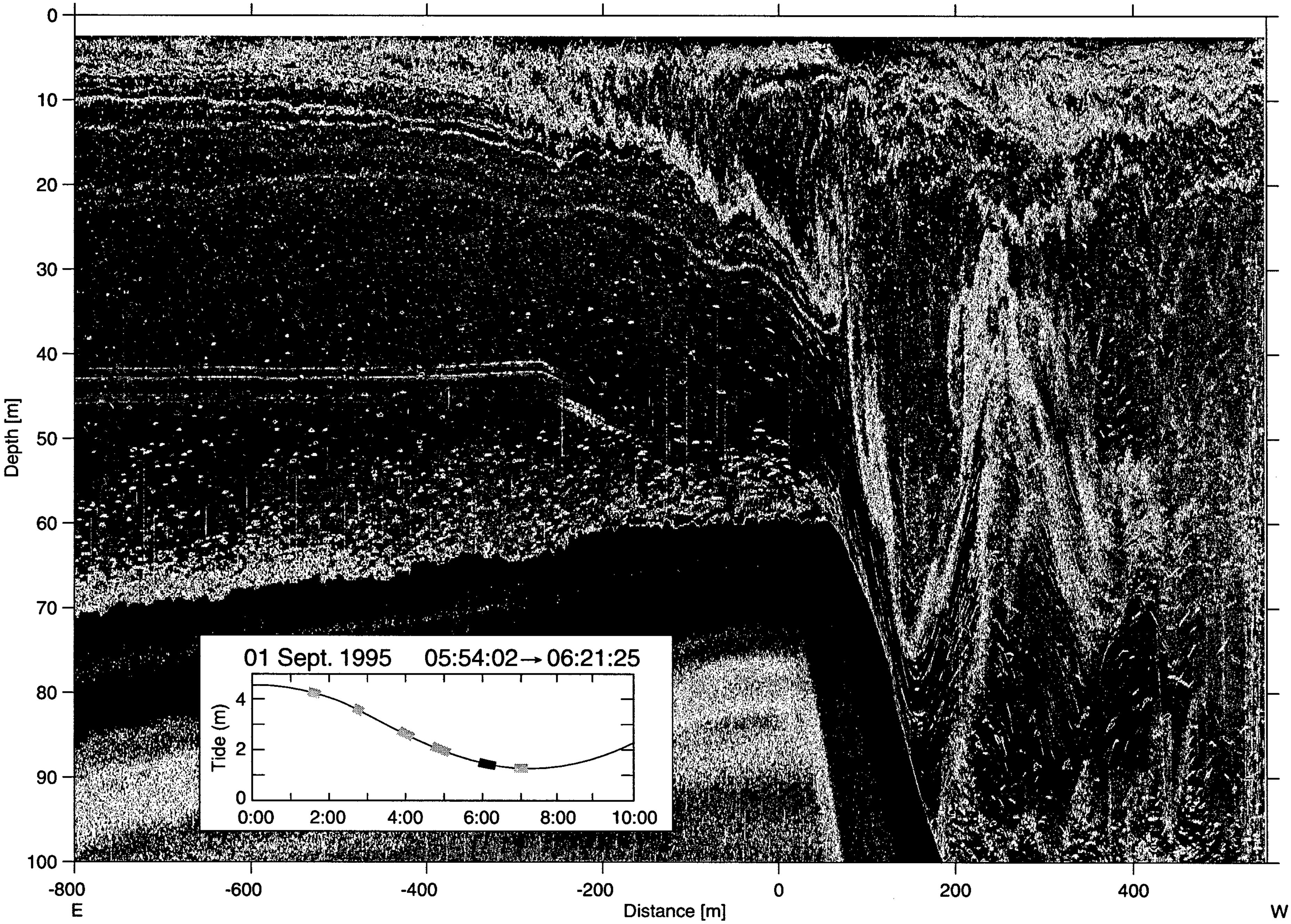
01 Sept. 1995 05:54:02→06:21:25
Tide (m)
0
2
4
0:00
2:00
4:00
6:00
8:00
10:00
Depth [m]
0
10
20
30
40
50
60
70
80
90
100
-800
-600
-400
-200
0
200
400
E
Distance [m]
W

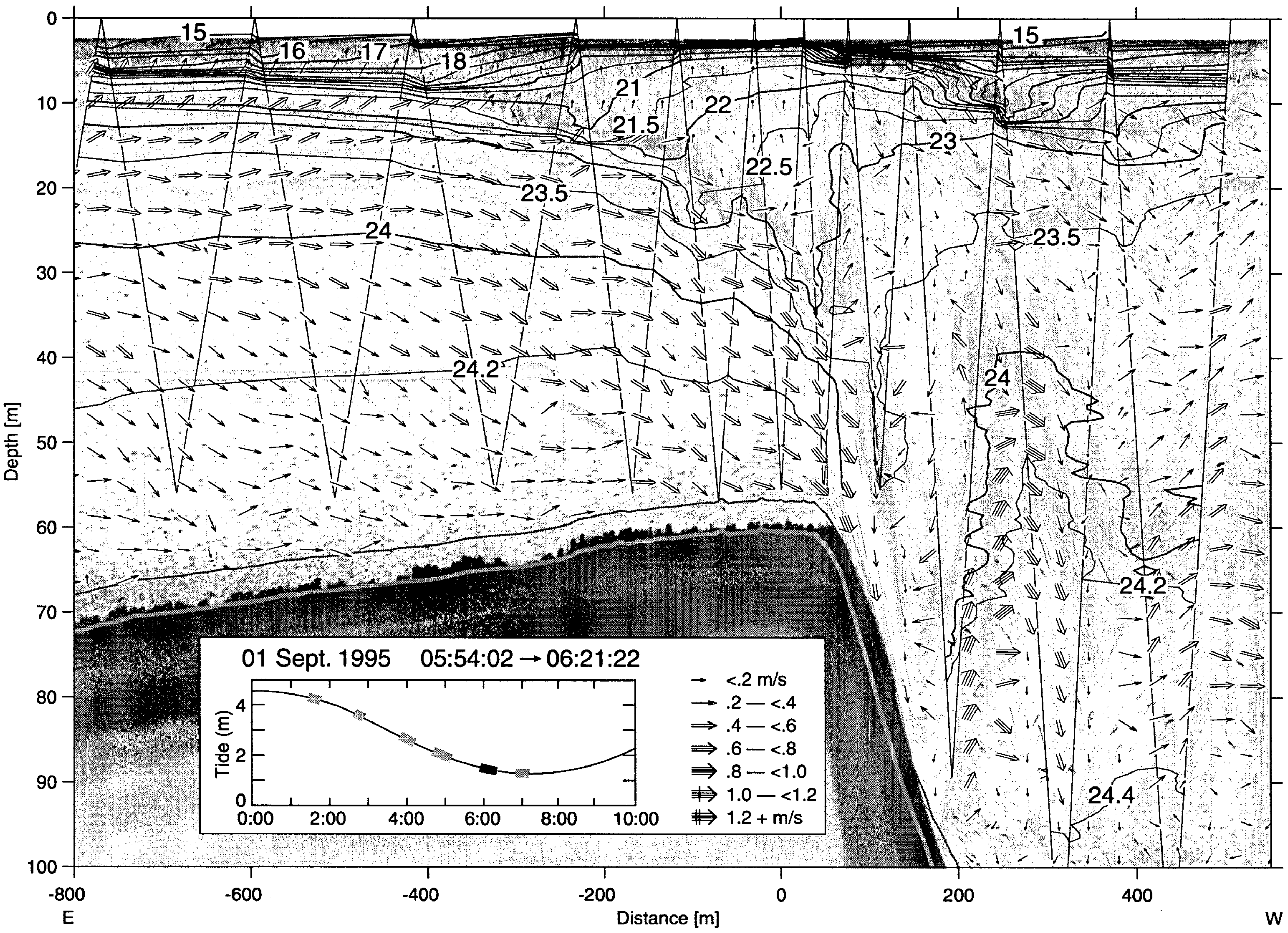
15
16
17
18
21
21.5
22
22.5
23
23.5
24
24.2
15
23.5
24
24.2
24.4
Depth [m]
0
10
20
30
40
50
60
70
80
90
100
-800
E
-600
-400
-200
0
200
400
W
Distance [m]
01 Sept. 1995 05:54:02 → 06:21:22
Tide (m)
0
2
4
0:00
2:00
4:00
6:00
8:00
10:00
<.2 m/s
.2 — <.4
.4 — <.6
.6 — <.8
.8 — <1.0
1.0 — <1.2
1.2 + m/s

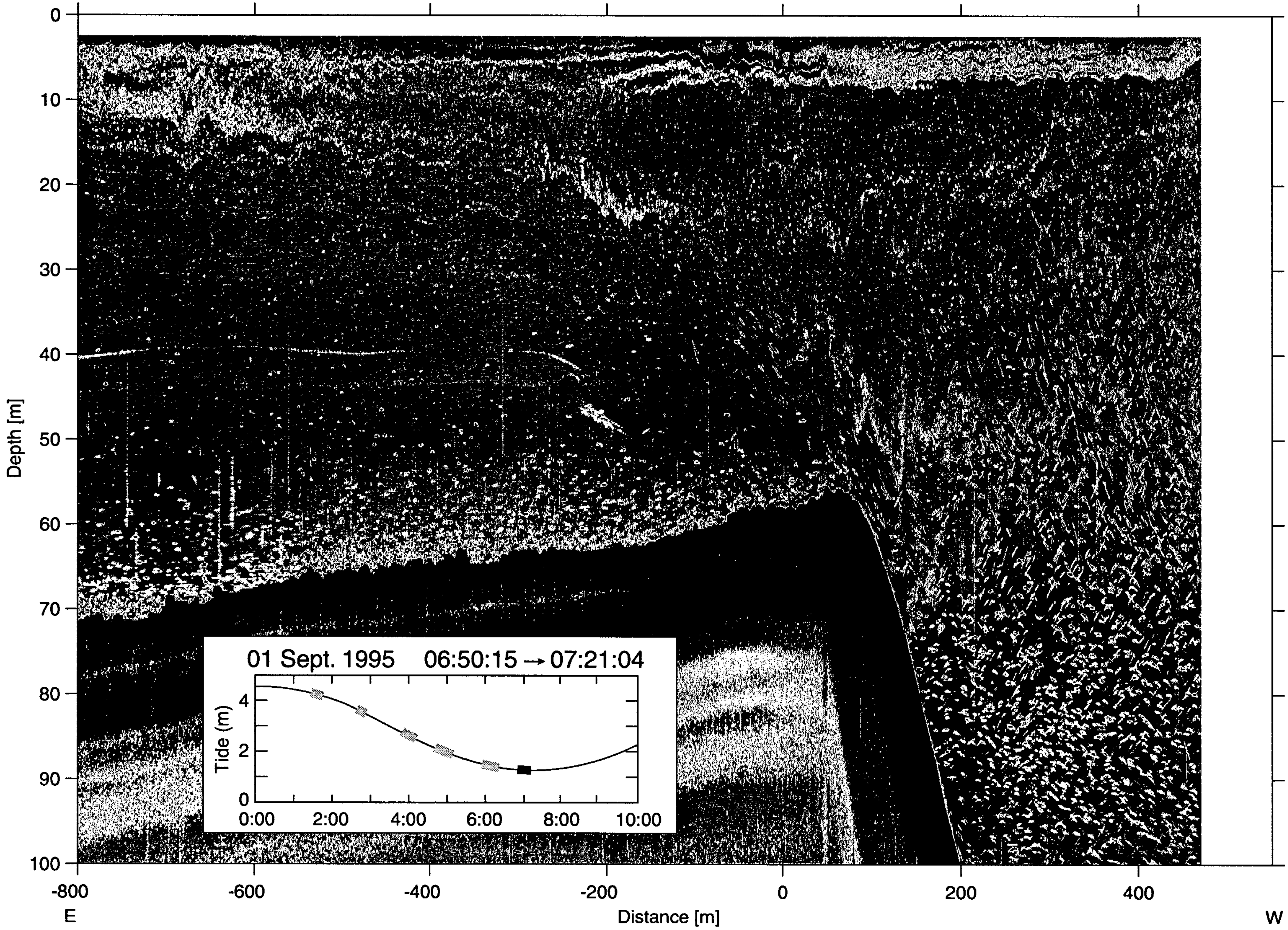
0
10
20
30
40
50
60
70
80
90
100
Depth [m]
-800
-600
-400
-200
0
200
400
E
Distance [m]
W
01 Sept. 1995   06:50:15 → 07:21:04
Tide (m)
0
2
4
0:00
2:00
4:00
6:00
8:00
10:00

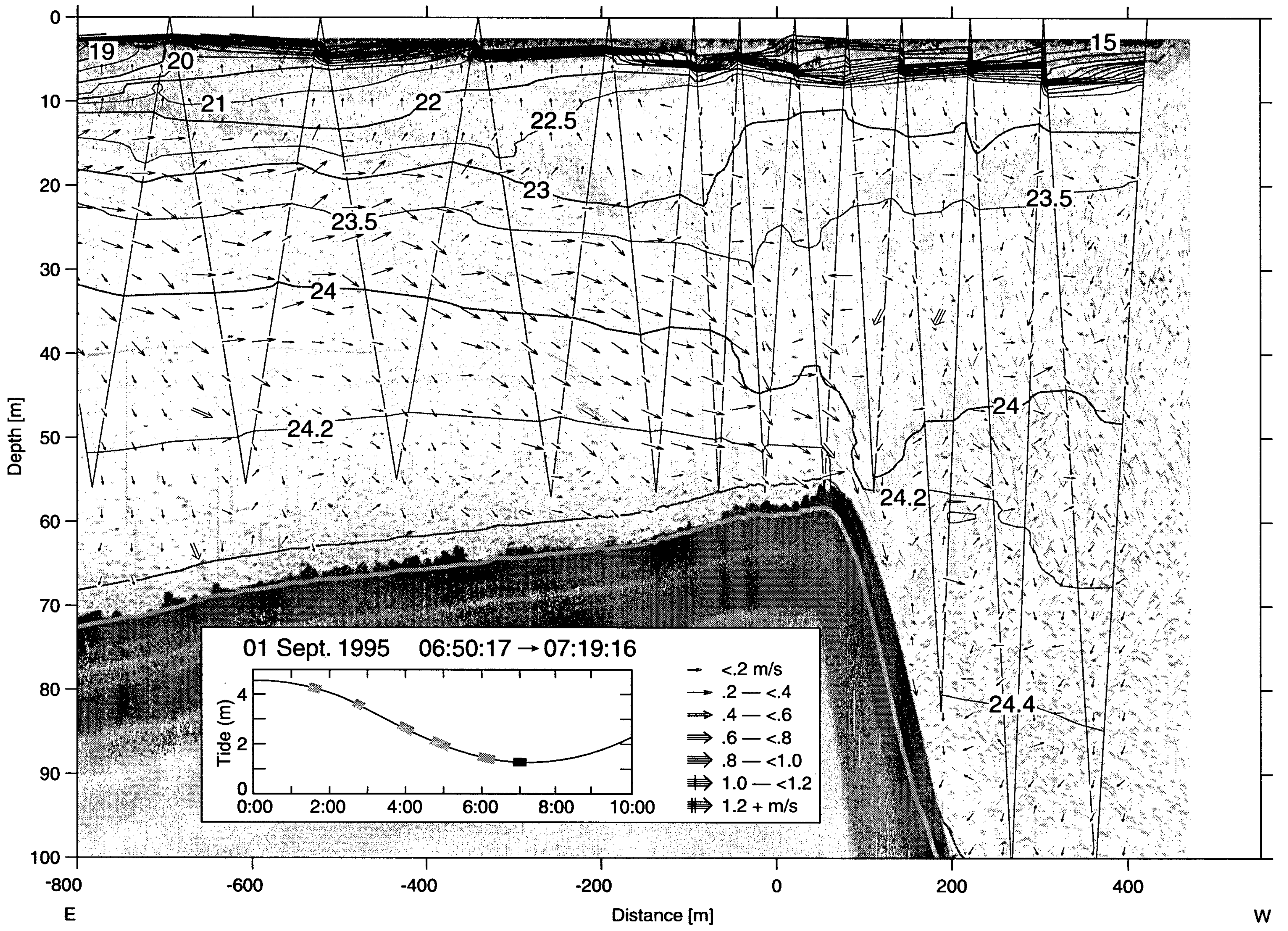

01 Sept. 1995 06:50:17 → 07:19:16
Depth [m]
Distance [m]
E
W
0
10
20
30
40
50
60
70
80
90
100
-800
-600
-400
-200
0
200
400
19
20
21
22
22.5
23
23.5
24
24.2
15
23.5
24
24.2
24.4
Tide (m)
4
2
0
0:00
2:00
4:00
6:00
8:00
10:00
<.2 m/s
.2 — <.4
.4 — <.6
.6 — <.8
.8 — <1.0
1.0 — <1.2
1.2 + m/s

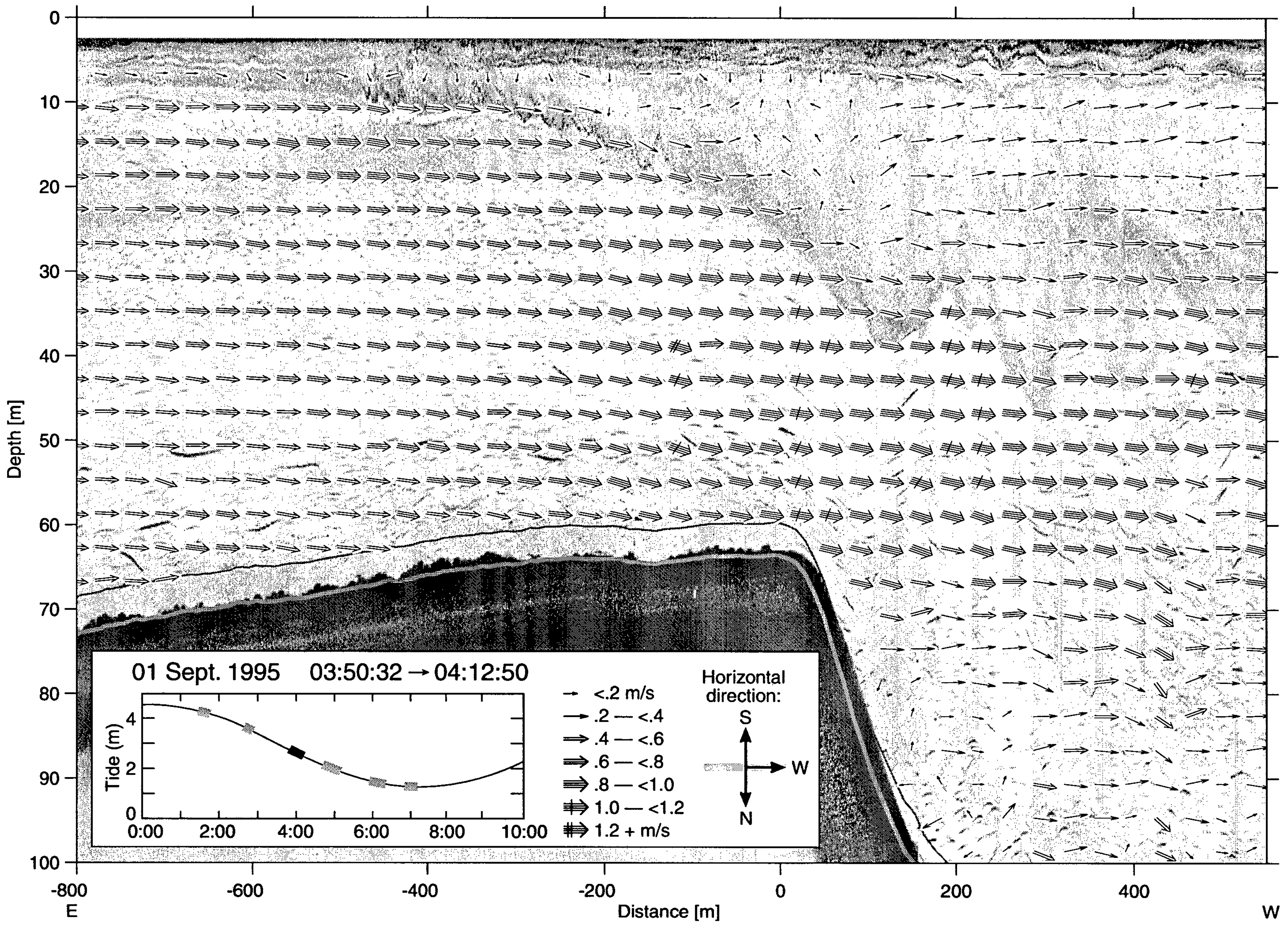
01 Sept. 1995 03:50:32 → 04:12:50
Tide (m)
0
2
4
0:00
2:00
4:00
6:00
8:00
10:00
<.2 m/s
.2 — <.4
.4 — <.6
.6 — <.8
.8 — <1.0
1.0 — <1.2
1.2 + m/s
Horizontal direction:
S
W
N
Depth [m]
0
10
20
30
40
50
60
70
80
90
100
-800
E
-600
-400
-200
0
200
400
W
Distance [m]

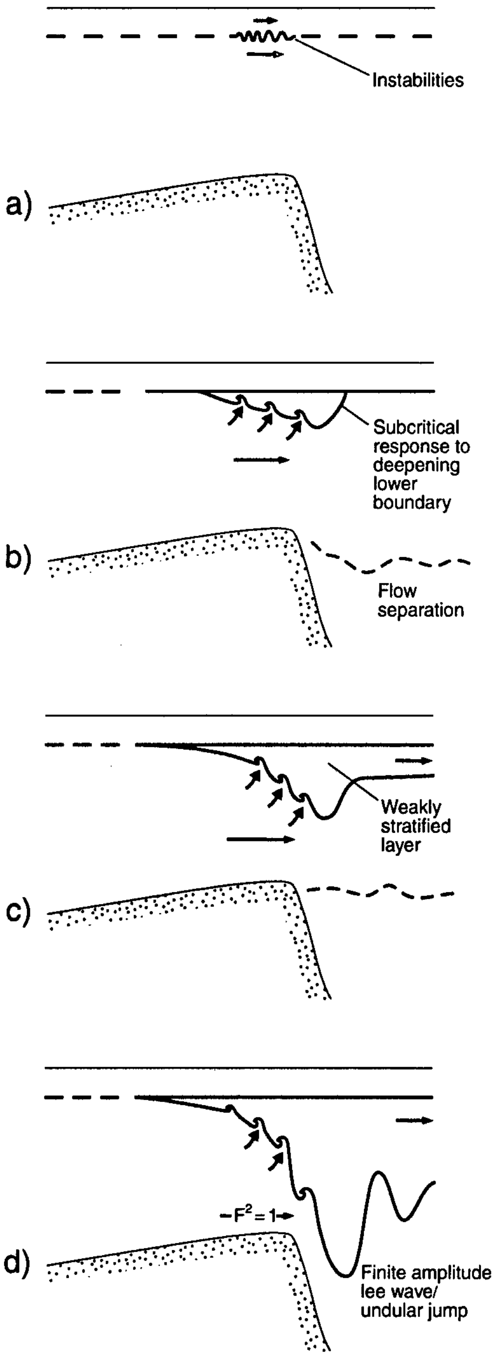
Instabilities
a)
Subcritical response to deepening lower boundary
b)
Flow separation
Weakly stratified layer
c)
−F² = 1→
Finite amplitude lee wave/ undular jump
d)

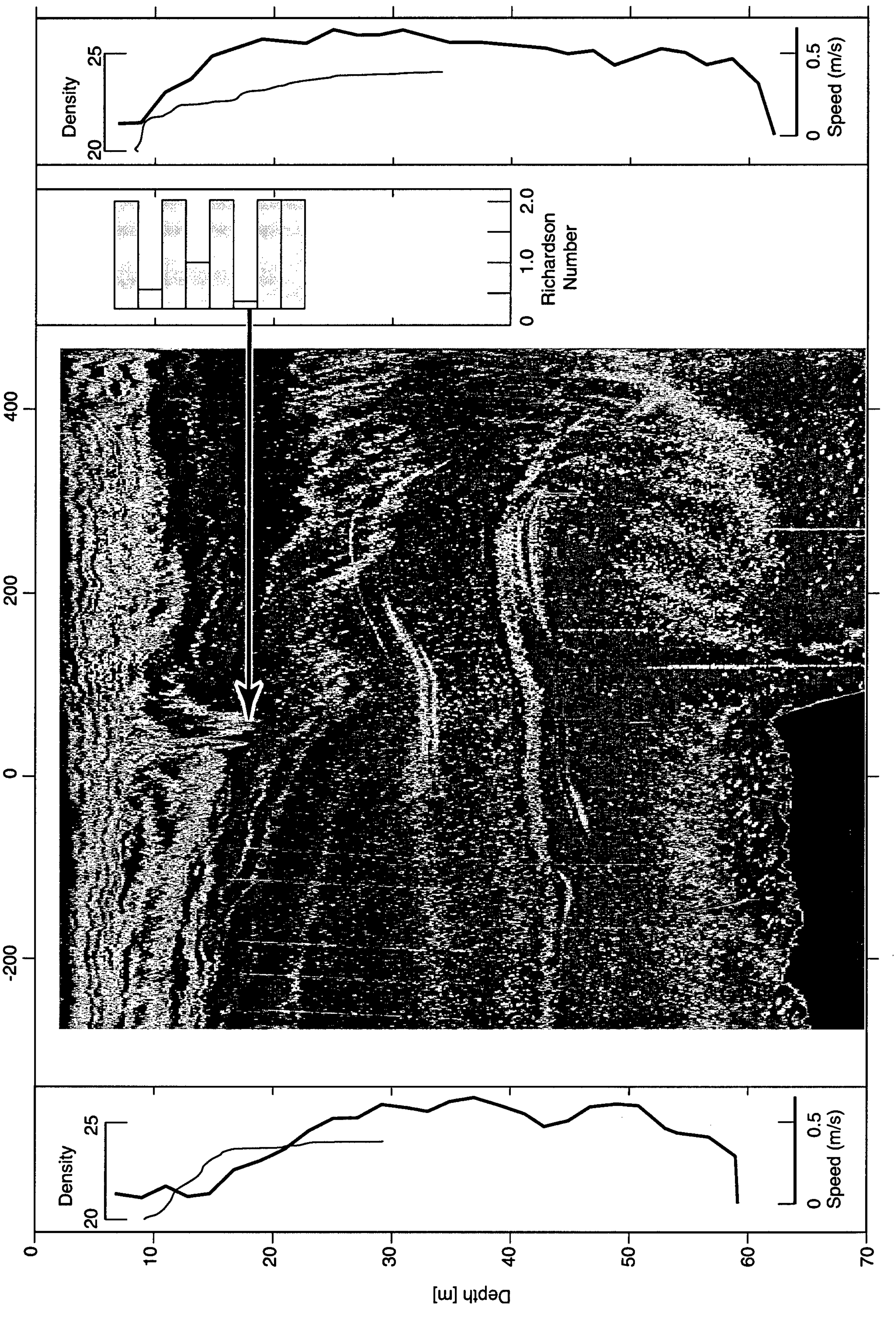
Density
20
25
Speed (m/s)
0
0.5
Richardson
Number
0
1.0
2.0
-200
0
200
400
Density
20
25
Speed (m/s)
0
0.5
Depth [m]
0
10
20
30
40
50
60
70

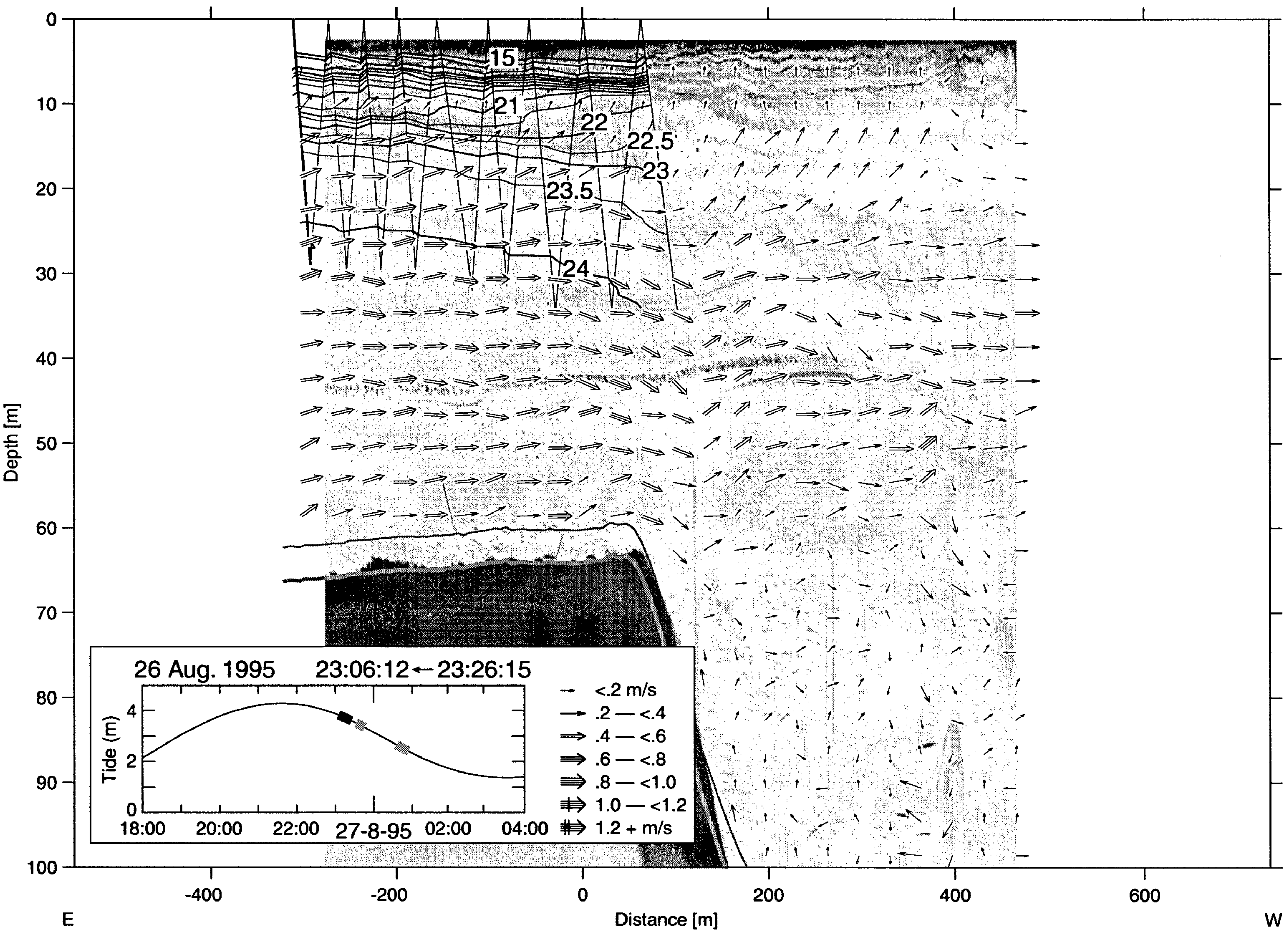

26 Aug. 1995
23:06:12←23:26:15
Tide (m)
0
2
4
18:00
20:00
22:00
27-8-95
02:00
04:00
<.2 m/s
.2 — <.4
.4 — <.6
.6 — <.8
.8 — <1.0
1.0 — <1.2
1.2 + m/s
15
21
22
22.5
23
23.5
24
Depth [m]
0
10
20
30
40
50
60
70
80
90
100
-400
-200
0
200
400
600
Distance [m]
E
W

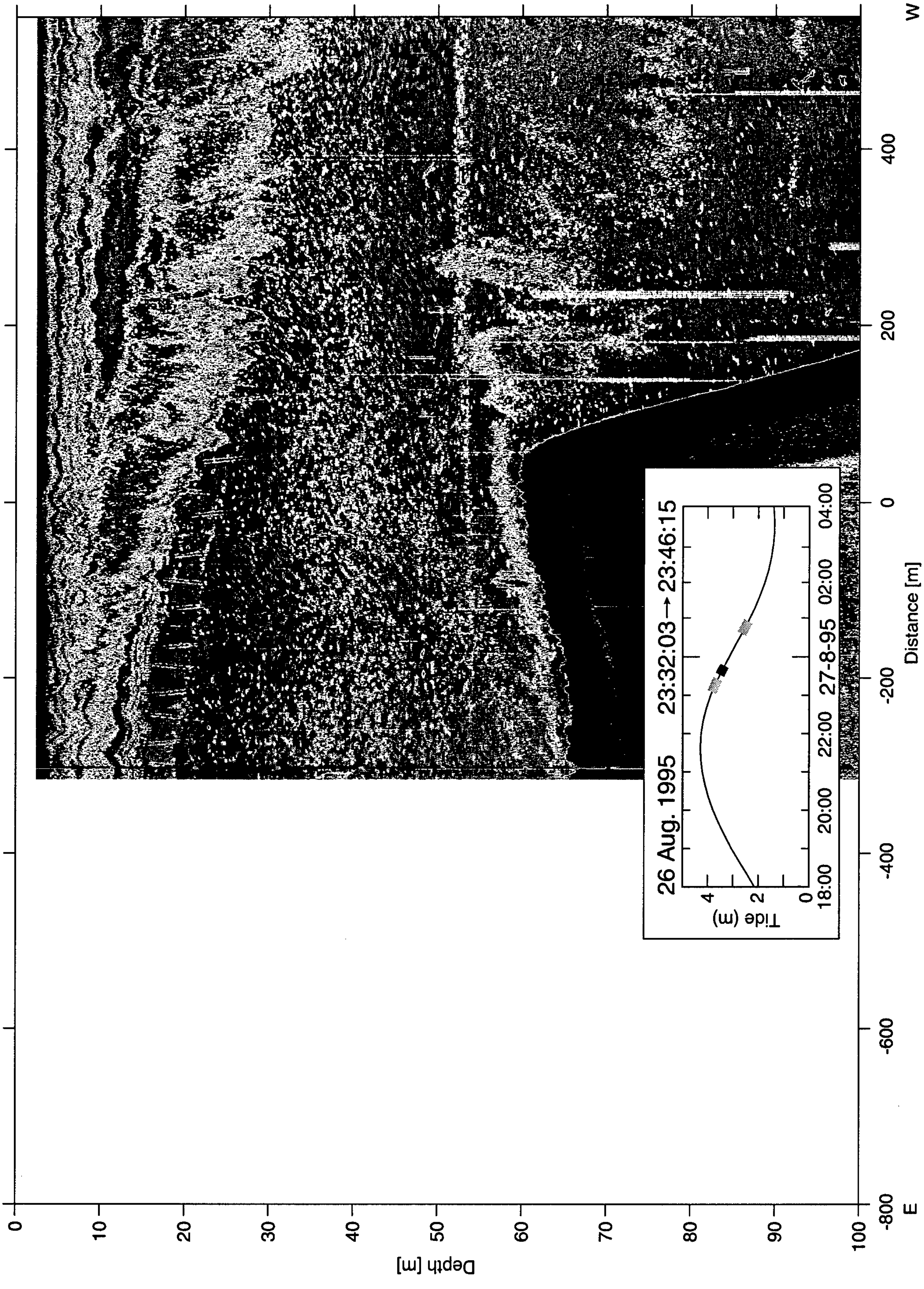
Depth [m]
0
10
20
30
40
50
60
70
80
90
100
Distance [m]
-800
-600
-400
-200
0
200
400
E
W
26 Aug. 1995 23:32:03→23:46:15
Tide (m)
0
2
4
18:00
20:00
22:00
27-8-95
02:00
04:00

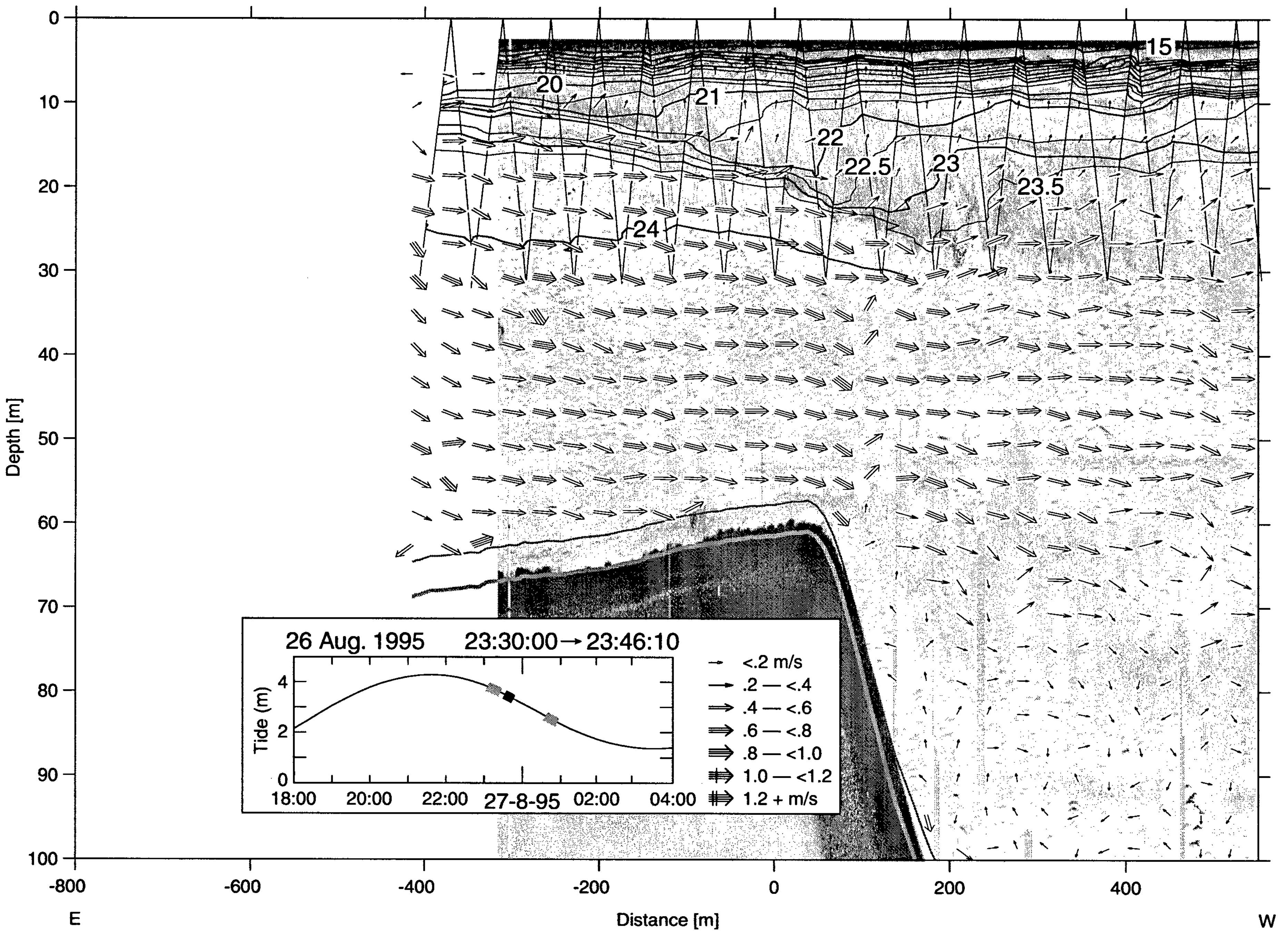

0
10
20
30
40
50
60
70
80
90
100
Depth [m]
-800
-600
-400
-200
0
200
400
E
Distance [m]
W
15
20
21
22
22.5
23
23.5
24
26 Aug. 1995
23:30:00→23:46:10
Tide (m)
4
2
0
18:00
20:00
22:00
27-8-95
02:00
04:00
<.2 m/s
.2 — <.4
.4 — <.6
.6 — <.8
.8 — <1.0
1.0 — <1.2
1.2 + m/s

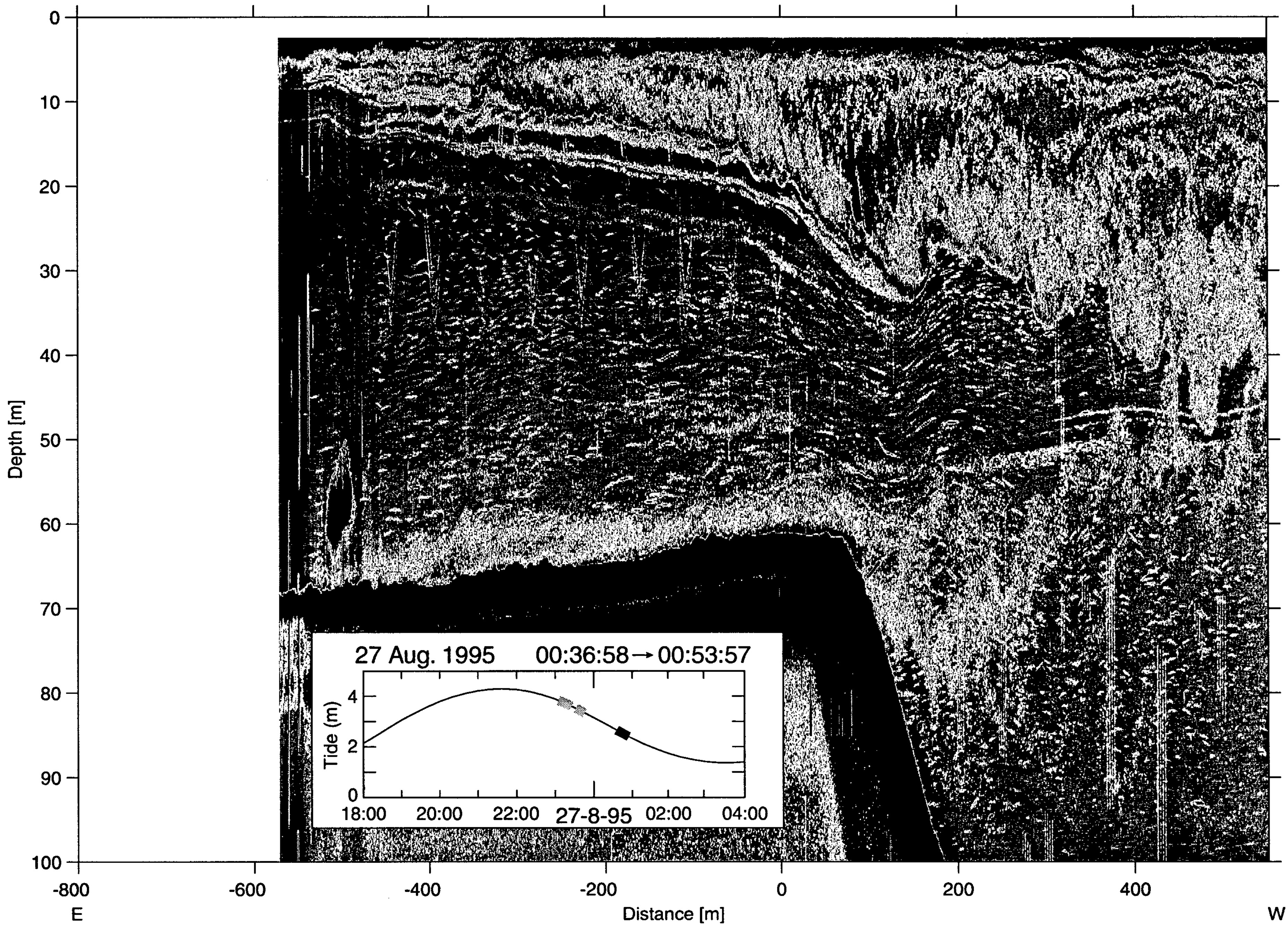

Depth [m]
0
10
20
30
40
50
60
70
80
90
100
-800
-600
-400
-200
0
200
400
E
Distance [m]
W
27 Aug. 1995
00:36:58→00:53:57
Tide (m)
0
2
4
18:00
20:00
22:00
27-8-95
02:00
04:00

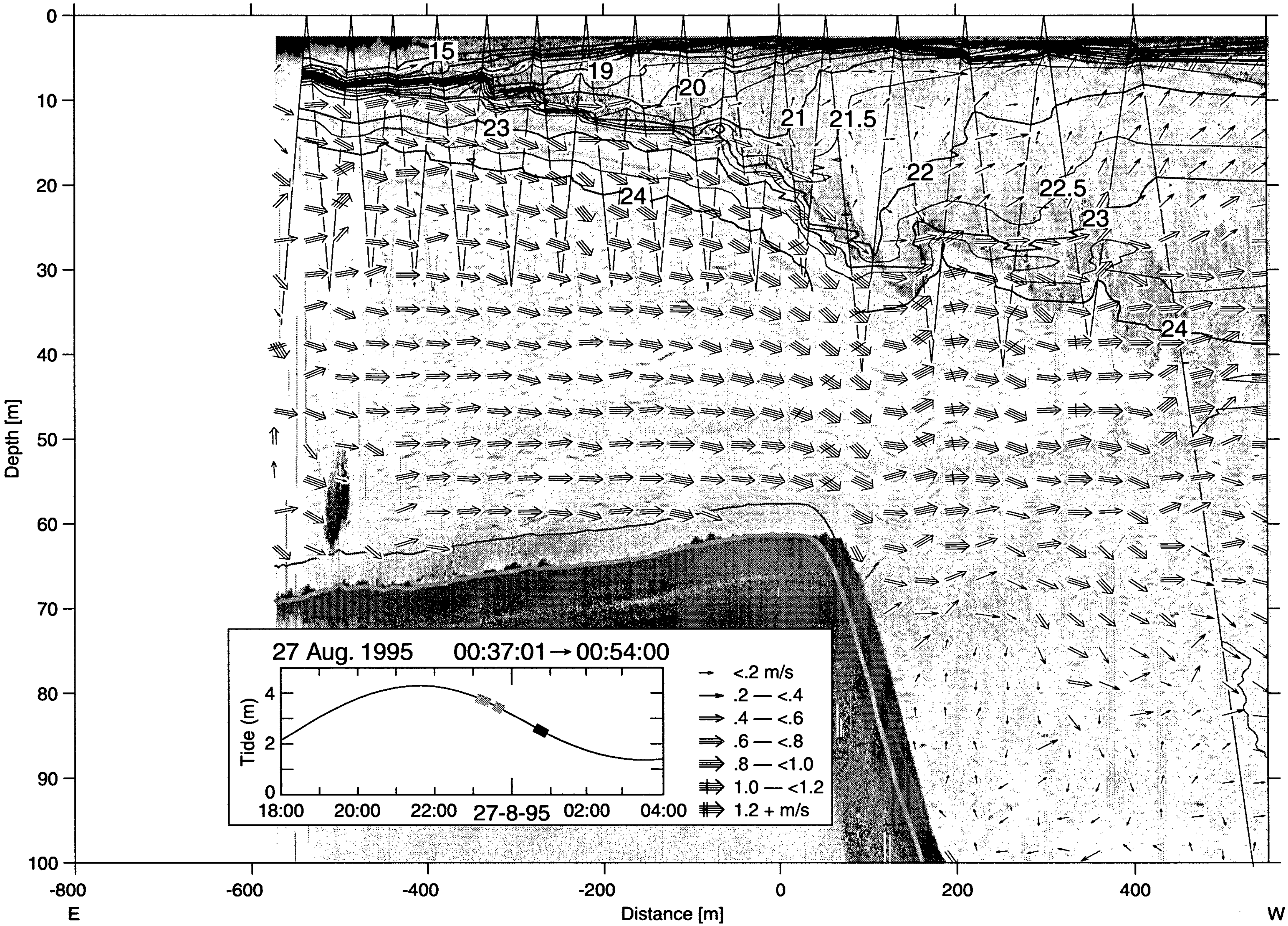
15
19
20
21
21.5
22
22.5
23
23
24
24
0
10
20
30
40
50
60
70
80
90
100
Depth [m]
-800
E
-600
-400
-200
0
200
400
W
Distance [m]
27 Aug. 1995 00:37:01 → 00:54:00
Tide (m)
4
2
0
18:00
20:00
22:00
27-8-95
02:00
04:00
<.2 m/s
.2 — <.4
.4 — <.6
.6 — <.8
.8 — <1.0
1.0 — <1.2
1.2 + m/s

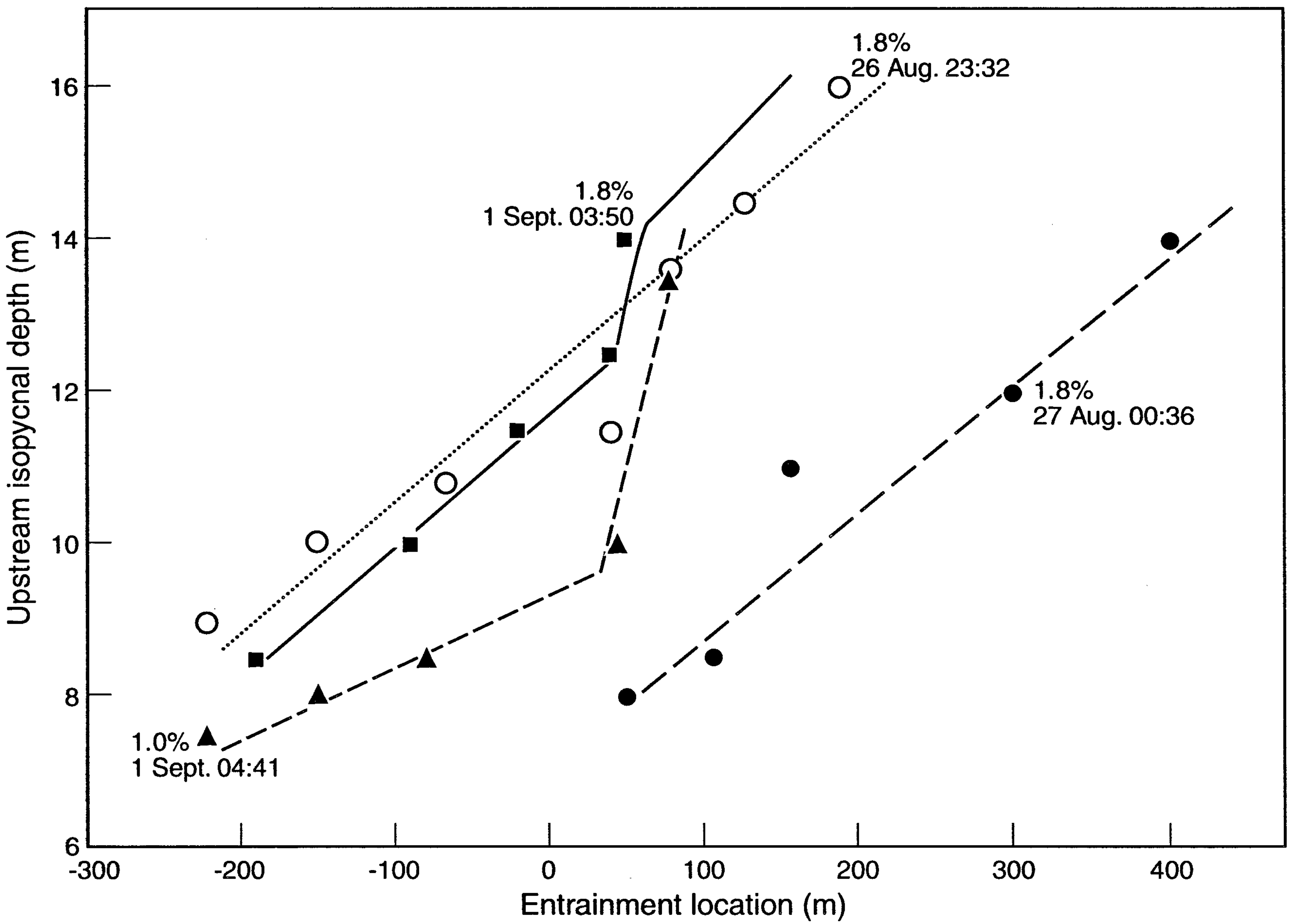
1.8%
26 Aug. 23:32
1.8%
1 Sept. 03:50
1.8%
27 Aug. 00:36
1.0%
1 Sept. 04:41
Upstream isopycnal depth (m)
16
14
12
10
8
6
-300
-200
-100
0
100
200
300
400
Entrainment location (m)

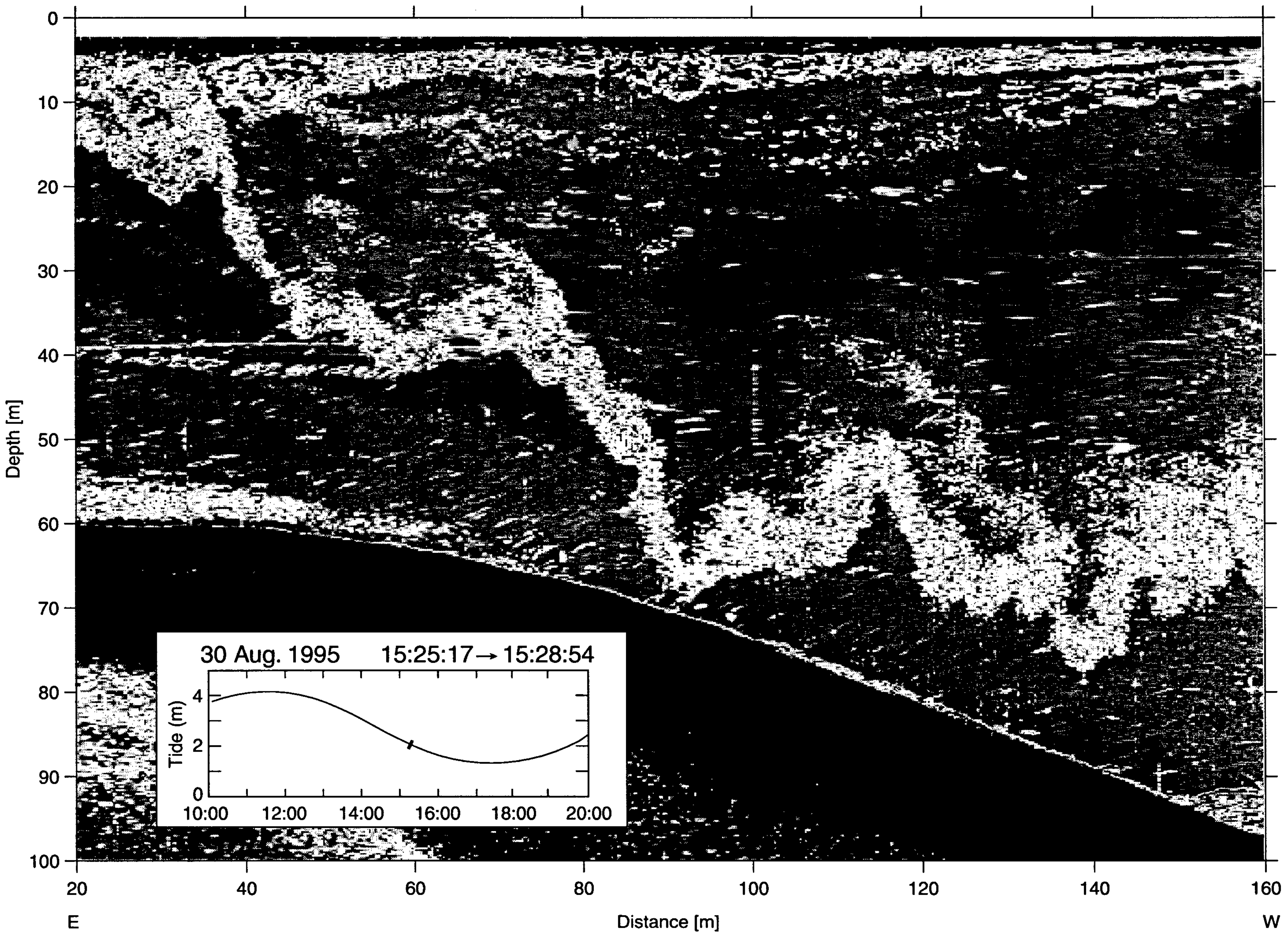

0
10
20
30
40
50
60
70
80
90
100
Depth [m]
20
40
60
80
100
120
140
160
E
Distance [m]
W
30 Aug. 1995
15:25:17 → 15:28:54
Tide (m)
4
2
0
10:00
12:00
14:00
16:00
18:00
20:00

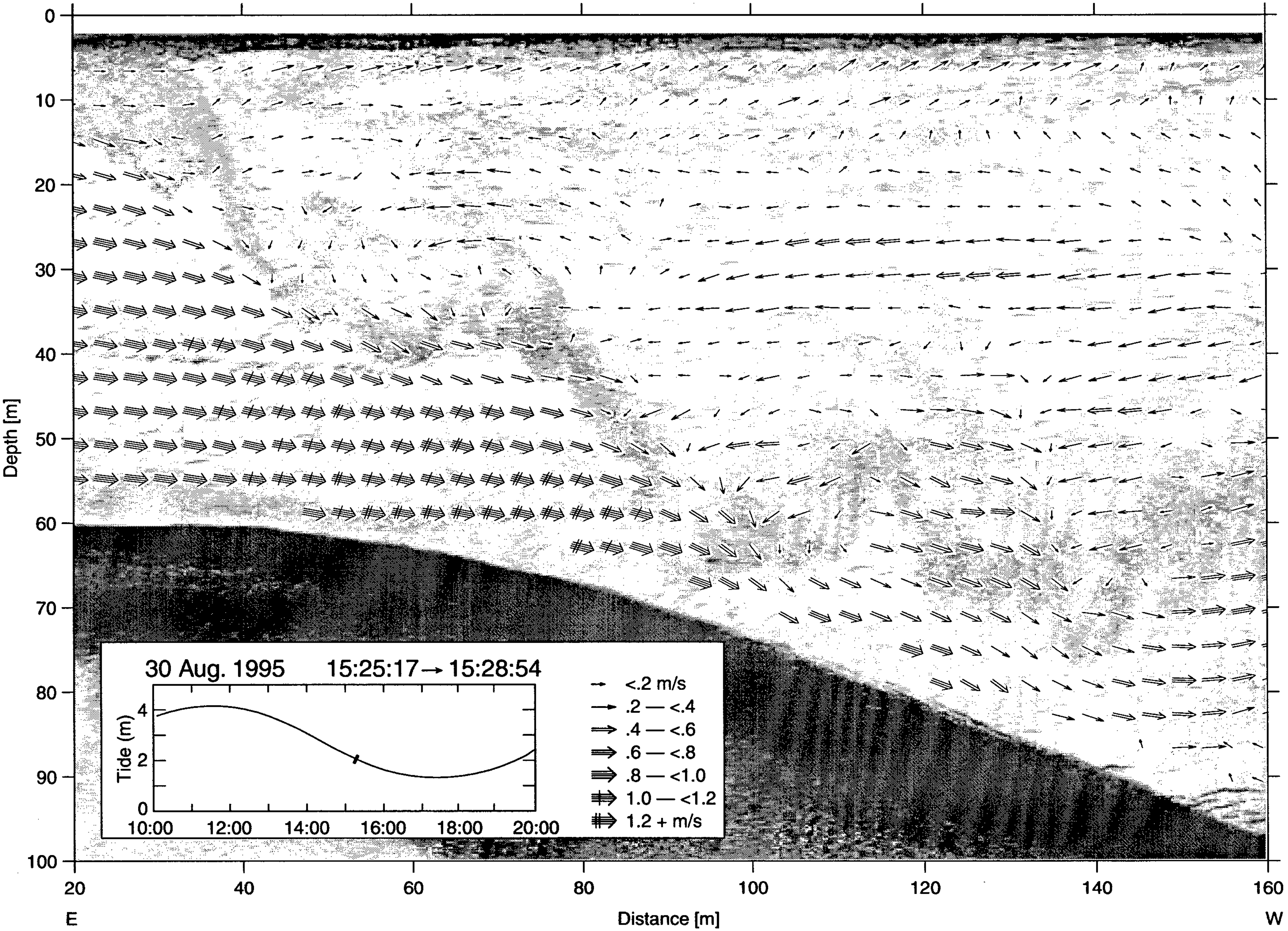
30 Aug. 1995 15:25:17→15:28:54
Depth [m]
0
10
20
30
40
50
60
70
80
90
100
Distance [m]
20
40
60
80
100
120
140
160
E
W
Tide (m)
0
2
4
10:00
12:00
14:00
16:00
18:00
20:00
<.2 m/s
.2 — <.4
.4 — <.6
.6 — <.8
.8 — <1.0
1.0 — <1.2
1.2 + m/s

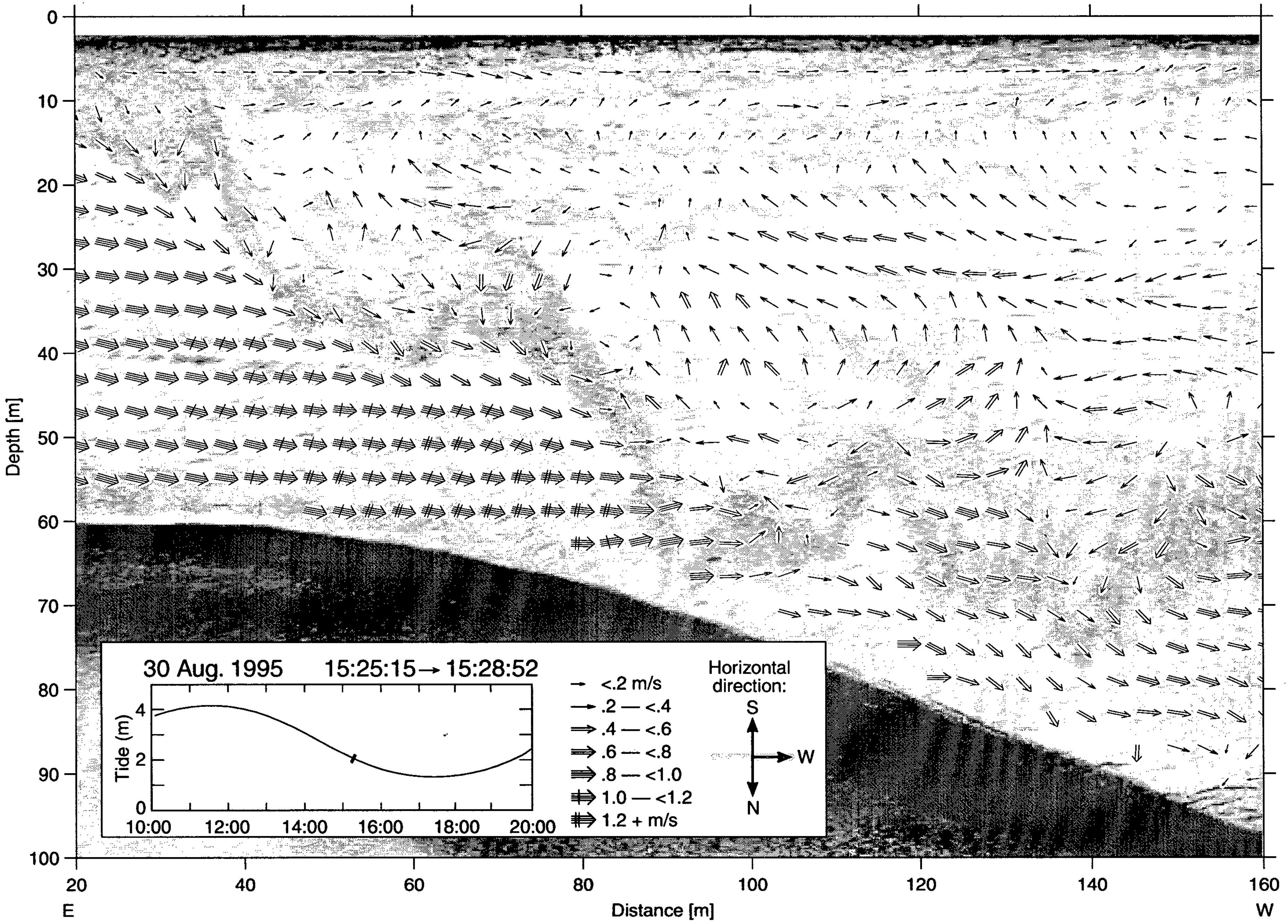
30 Aug. 1995 15:25:15→ 15:28:52
Tide (m)
4
2
0
10:00
12:00
14:00
16:00
18:00
20:00
<.2 m/s
.2 — <.4
.4 — <.6
.6 — <.8
.8 — <1.0
1.0 — <1.2
1.2 + m/s
Horizontal direction:
S
W
N
Depth [m]
0
10
20
30
40
50
60
70
80
90
100
Distance [m]
20
40
60
80
100
120
140
160
E
W

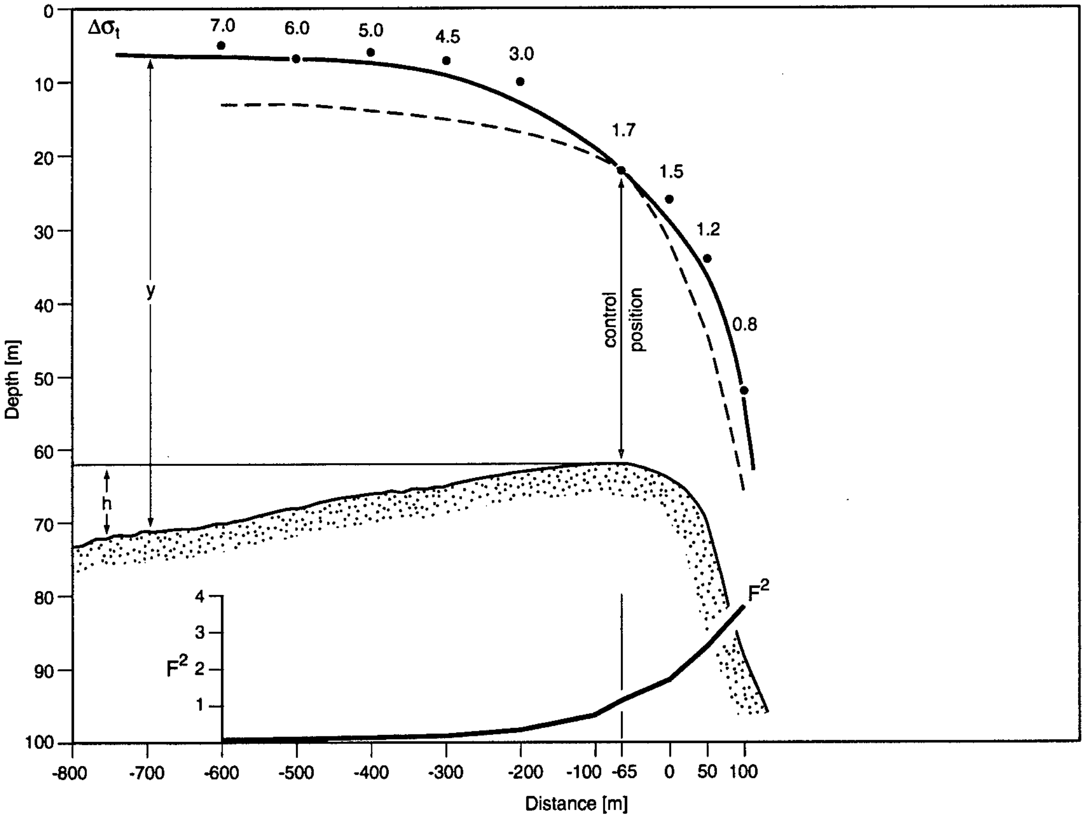

$\Delta\sigma_1$
7.0
6.0
5.0
4.5
3.0
1.7
1.5
1.2
0.8
y
h
control position
F^2
Depth [m]
0
10
20
30
40
50
60
70
80
90
100
4
3
2
1
-800
-700
-600
-500
-400
-300
-200
-100
-65
0
50
100
Distance [m]

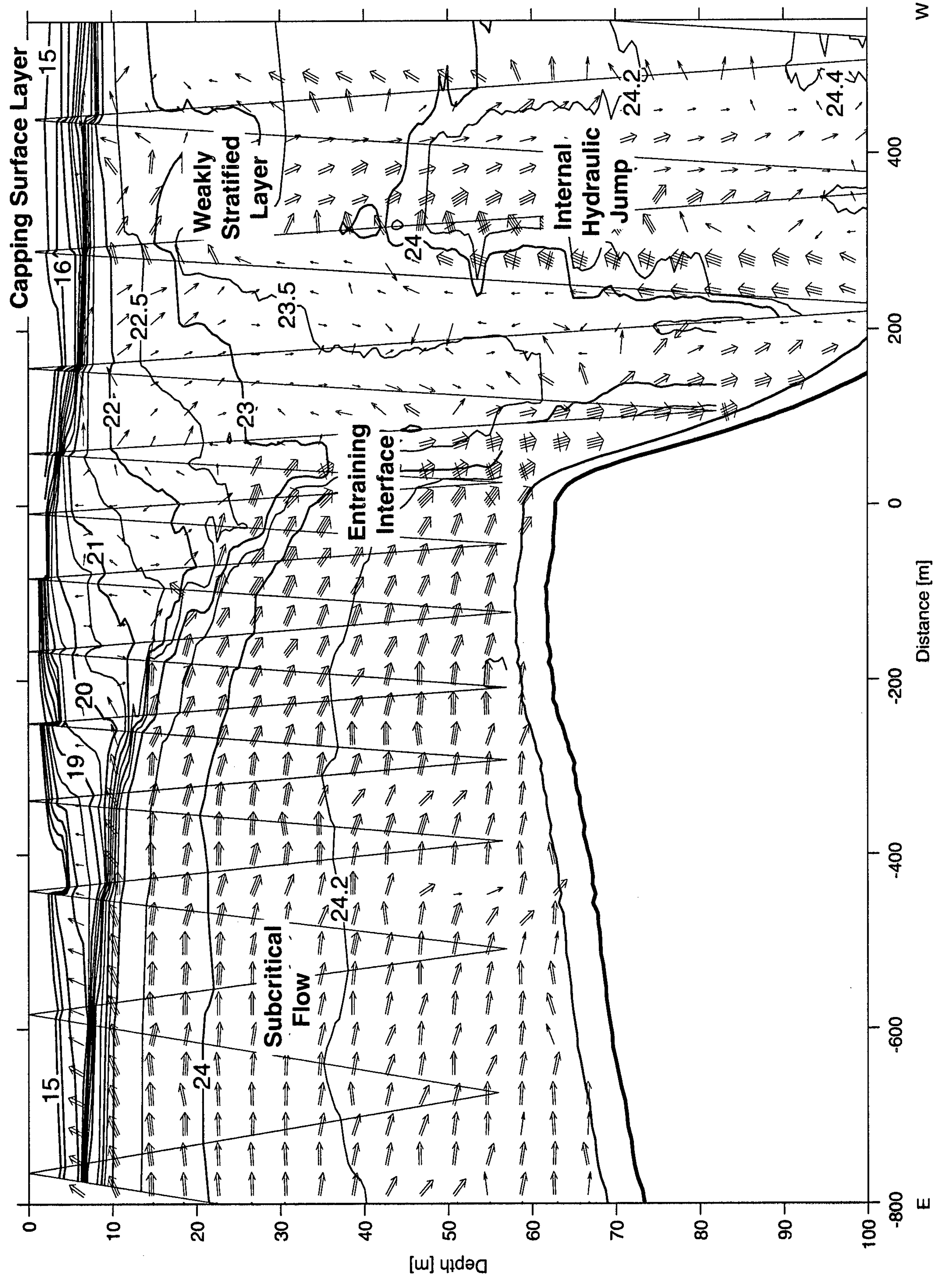
Capping Surface Layer
Weakly Stratified Layer
Internal Hydraulic Jump
Entraining Interface
Subcritical Flow
15
16
19
20
21
22
22.5
23
23.5
24
24.2
24.4
Depth [m]
0
10
20
30
40
50
60
70
80
90
100
Distance [m]
-800
-600
-400
-200
0
200
400
E
W